JUMR

Journal of Undergraduate Materials Research

"The Voice of Future Scientists and Engineers"

The Science of Sound

The Power of Microwaves

Featuring Research From

South Dakota School of Mines

Rose-Hulman Institute

University of Hartford

IIT, Chennai, India

Virginia Tech

Georgia Tech

Wright State

A Publication of the Department of
Materials Science and Engineering at Virginia Tech
Volume 4 | Spring 2010

Dear Friends,

We are pleased to present the fourth volume of the Journal of Undergraduate Materials Research (JUMR). Since the release of the Alfred E. Knobler inaugural issue in the Fall of 2005, JUMR has continued to showcase undergraduate research in the field of Materials Science and Engineering (MSE). Volume 4 focuses on the benefits of collaborative learning at the undergraduate level between multiple universities and industries.

We thank all of the students who submitted for publication. The competitive process includes review by faculty and graduate students from universities as well as professionals from industry. Congratulations to the student authors whose papers were accepted for this volume. This publication includes work by students from universities in the United States and India, including Virginia Polytechnic Institute and State University, University of Hartford, Rose-Hulman Institute of Technology, Wright State University, South Dakota School of Mines, Georgia Institute of Technology, and Indian Institute of Technology in Chennai, India.

Many of these student authors have achieved national recognition by participating in the JUMR symposium at MS&T'09 (October 26, 2009, Pittsburgh, PA). Due to a prodigious amount of interest in the JUMR symposium, a second session was added to accommodate all of the submissions. We anticipate the same enthusiastic response for the MS&T'10 JUMR symposium.

Finally, the Editorial Board thanks our reviewing committee, our faculty advisors, and especially our readers for their continued support. We are accepting manuscripts for Volume 5. Additionally, the articles not included in Volume 4 will be reconsidered for publication in Volume 5.

Sincerely,

The Editorial Board

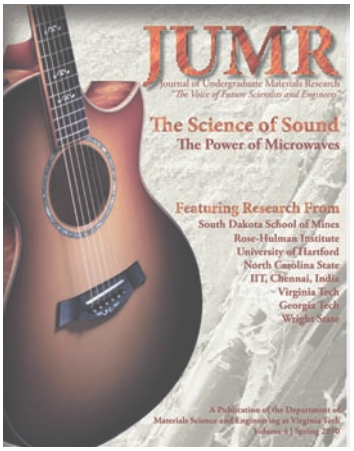

On the Cover:

Taylor's Grand Concert Guitar with micrograph from "*Microwave Processing of Polymeric Coatings for Guitar Woods*" (see pg. 12). Instrument photograph provided by Taylor Guitars, El Cajon, CA.

Back Row (L-R): Niklas Floyd, Manoj Mahapatra, Raghunath Thridandapani, David Berry, Katelyn Webster, Andrea Rojas, Kristen Zimmermann
Front Row: Tongan Jin, Susan Holt, Charles Sprinkle
Not Pictured: Aimee Gervacio, Dennis Hollich, Tyler Horseman, Niven Monsegue

Materials Science and Engineering
discover what we're made of...

Journal of Undergraduate Materials Research (ISSN 1934-7677)

FEATURE ARTICLES

FEATURED DEPARTMENTS

RESEARCH ARTICLES

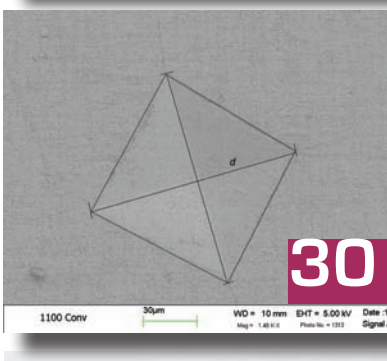

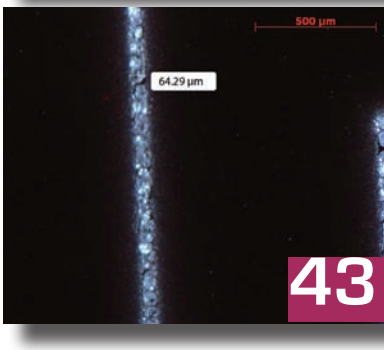

EDITORIAL CREDITS

FACULTY REVIEWERS

Samuel Henry, *University of Oxford*
Behnam Pourdeyhimi, *North Carolina State University*
Kalayanee Kooptarnond, *The Pennsylvania State University*
Morsi Mahmoud, *Advanced Technologies and New Materials Research Institute, Egypt*
Thomas Nosker, *Rutgers University*
Carl Boehlert, *Michigan State University*
Yaowu Hao, *University of Texas at Arlington*
Ranabrata Mazumder, *NIT Rourkela, India*
Alex Aning, *Virginia Tech*
Jeremiah Abiade, *Virginia Tech*
Stephen Kelly, *Johns Hopkins University*
William Johnson, *University of Virginia*
Scott Case, *Virginia Tech*
Ishwar Puri, *Virginia Tech*

GRADUATE STUDENT REVIEWERS

Reza Montazami, *Virginia Tech*
Rahul Lodha, *University of Columbia*
Stephen Bottiglieri, *The State University of New Jersey*
Patrick Aderhold, *Michigan State University*
Chenlin Zhao, *Virginia Tech*
Amit Amritkar, *Virginia Tech*

INDUSTRY REVIEWERS

Abhoy Kumar, *Defense Metallurgical Research Laboratory, India*
Adrish Ganguly, *Williams Advanced Materials, New York*
Anal Tarafder, *Central Glass and Ceramic Research Institute, India*

JUDGES

Rebecca Schulz, *Corning Incorporated*
Nitin Chopra, *University of Alabama*

SPECIAL THANKS

Louis Manzione, Dean
College of Engineering, Technology and Architecture, University of Hartford
David Clark, Professor and Head
Materials Science and Engineering, Virginia Tech
Carolyn Rude, Professor and Chair
English, Virginia Tech
Lindsey Kincaid, Undergraduate Student
Art, Emory & Henry College

STUDENT EDITORIAL BOARD

Editor-in-Chief	Raghu Thridandapani Graduate Student, Materials Science and Engineering
Associate Editor	Manoj Mahapatra Graduate Student, Materials Science and Engineering
Design Editors	Charles Sprinkle Graduate Student, Materials Science and Engineering
	Katelyn Webster and Aimee Gervacio Undergraduate Students, English
Peer Review Organizers	Kristen Zimmermann Graduate Student, School of Biomedical Engineering and Sciences
	Niklas Floyd and David Berry Graduate Students, Materials Science and Engineering
Finance Manager	Tongan Jin Graduate Student, Materials Science and Engineering
Public Relations	Andrea Rojas Graduate Student, Materials Science and Engineering
Data Manager	Susan Holt Graduate Student, Materials Science and Engineering
Undergraduate Liaison	Dennis Hollich Undergraduate Student, Materials Science and Engineering
Photographer	Niven Monsegue Graduate Student, Materials Science and Engineering
General Board Member	Tyler Horseman Graduate Student, Materials Science and Engineering

FACULTY EDITORIAL BOARD

JUMR Faculty Advisor	Diane Folz Materials Science and Engineering
Industry Advisor	Ben Poquette *Keystone Materials, LLC*
Materials Science and Engineering, Faculty	Jeremiah Abiade Alex Aning
Department of Electrical and Computer Engineering, Faculty	Patricia Mellodge *University of Hartford*
Engineering Science and Mechanics, Materials Science and Engineering, Faculty	Christine Burgoyne
English Faculty	Steve Kark

Letter from the Department Head

David Clark, Materials Science and Engineering

Dear Students and Colleagues:

I am pleased with the positive response that JUMR has received from the materials community. In the first three issues, we have published 27 high-quality papers authored by undergraduate students from the United States and abroad. All classes of materials are represented, covering a wide array of applications such as energy, health, sports, and manufacturing. JUMR is truly a grassroots, student-driven publication that provides a unique forum for undergraduate students to present their research. It also provides an excellent opportunity for graduate students serving on the editorial board to get firsthand experience creating a technical journal. The quality of the first three issues is superb in terms of technical content and visual appeal; this issue is no exception.

The theme of this issue is collaborative learning between multiple universities and industries. It is amazing to see the creative ideas that can evolve when very different disciplines work together to solve problems and produce new technology. Biomedical engineering is a good example of this type of effort. Its roots go back over 40 years when faculty from the medical and engineering professions began collaborating on new replacement materials for the human body, and continues today with the design of new drug delivery systems. The unique aspect of collaborative learning described in this issue is that it is driven by the undergraduate students. The program, as it is being developed, can be adopted by any university/discipline.

A particularly fascinating example of this collaboration is demonstrated in the paper entitled, "Microwave Processing of Polymeric Coatings for Guitar Woods." Undergraduate students from the University of Hartford and Virginia Tech are working with a major guitar manufacturer to reduce production costs and produce a superior product. These types of collaborations are exciting to the students involved in the research and can interest high school and first-year college students to pursue materials research.

I am pleased with the support that JUMR has received from the materials professional societies. For the last three years, JUMR has partnered with the organizers of MS&T to run a symposium for undergraduate research. The symposium will be held again this year at the MS&T'10 meeting in Houston, Texas. Abstracts have already been received from undergraduates at universities in the United States, Egypt, and India.

Many of the journal articles and symposium presentations are based on senior design projects, while a few represent the work of a student conducting independent research. These articles and presentations illustrate the variety of research opportunities that MSE programs are providing to undergraduates. It is gratifying to see the quality of research that undergraduates are producing in addition to the communication and team-building skills that they are developing in their materials curricula. This student work is an excellent reflection on the faculty in our discipline.

The materials community has always been a close group, working together and sharing ideas that have made us stronger. I believe that JUMR has the potential to build upon this foundation. I encourage undergraduate students, graduate students, and faculty from all universities and industries to become involved with JUMR activities. We expect to receive papers from a wider range of universities. We anticipate engaging a higher number of graduate students, faculty, and industry representatives to participate in reviewing the manuscripts and to serve on the editorial board. I can speak for all those who have been involved thus far when I say that they have found it to be a rewarding experience.

Sincerely,

David E. Clark
Professor and Head
Materials Science and Engineering
Virginia Tech

Collaborative Learning

Enhancing the Undergraduate Research Experience

Katelyn Webster and Aimee Gervacio
Virginia Polytechnic Institute and State University, English Department, Blacksburg, Virginia 24061

Music has always united people through concerts, operas, and campfires. For two universities, music brings together undergraduate students despite 615 miles of separation.

Engineering students at Virginia Tech and the University of Hartford are working together on a music-inspired project that hopes to discover a new method for coating guitars. While this project connects the fields of engineering and the arts, it also yields benefits for students and faculty through collaborative learning efforts.

The Project

Seven years ago, Ms. Diane Folz (Materials Science Engineering (MSE), Virginia Tech) and Dr. Patricia Mellodge (Electrical and Computer Engineering, University of Hartford) worked together in the Microwave Processing Research Facility in the MSE department of Virginia Tech. Sharing a love of guitars, Folz and Mellodge envisioned a guitar-based microwave processing project.

As ideas for the project developed, Mellodge joined the engineering department at the University of Hartford. Throughout this transition, Folz and Mellodge continued to research and visit guitar companies to learn more about guitar-building and finishing. Finally, they achieved success after Taylor Guitar Company enthusiastically agreed to work with them.

Taylor Guitars welcomed the collaboration. Matt Guzzetta, Senior Industrial Designer, stated that, “one great thing about experimentation is that you may discover something along the way totally unexpected.”

For Folz and Mellodge, the initial idea behind building a collaborative learning project was to work with undergraduate students. By combining the resources of each

Various guitar body sides are shaped using special heated platens. Here, they are stacked and awaiting backs and tops.

university, the benefits were endless. The University of Hartford has an acoustical engineering program and a lab in which vibrational testing could be performed on the samples made at Virginia Tech.

Dr. Bob Celmer, the director of the Acoustical Engineering program at the University of Hartford, became interested in working on the project and having his undergraduate students involved as well. According to Celmer, "the collaboration gives each group a unique perspective that is not achievable by any other approach. There are both synergies as well as realizations of the 'bigger picture', wherein both groups are the beneficiaries." As a result, this opened up a huge opportunity for the Virginia Tech researchers who could now work with their undergraduate counterparts in an acoustical program.

Meanwhile, the microwave laboratory at Virginia Tech is unique in that this technology is not widely researched in academia. The Virginia Tech researchers are well-known internationally for their expertise in this area of materials processing. Additionally, the University of Hartford does not have a materials engineering program, so the participating students of both schools gain appreciation for other fields of engineering.

Why Work Together?

Embarking on a collaborative learning project produces many benefits for students, faculty members, and industries. It provides students with the opportunity to take their education to the next level and to see where their education fits into the real world of engineering and other fields. More so, the project provides the students with a broader perspective of their profession and improves their understanding of how the real world works, which ultimately makes them better prepared to work as engineers after they graduate.

Mellodge states that, "the students get to see how colleagues who are working on the project contribute, but with a different focus. In any project, there are many aspects to it and different groups of people need to contribute their part for it to be successful." As a result, students benefit from collaborative learning experiences through interactions with colleagues from different departments and disciplines.

Likewise, faculty members benefit in the same way. By working with colleagues from a different discipline, they expand their knowledge and breadth of understanding of real world engineering issues. This knowledge then carries over to improve their teaching and work on other projects. Folz agrees that, "despite [a lack of] funding, passion sparks collaborative learning and keeps the fire alive."

Companies such as Taylor Guitars benefit from this collaboration because it increases the number of experts they have working on a research problem.

Lou Manzione, Dean of College of Engineering, Technology, and Architecture at the University of Hartford, agrees that Taylor Guitars benefits from this collaborative learning in today's ultra-competitive environment. "Very few companies have the resources to conduct all the basic research they would like to do. It allows them to save time and money on an issue that they otherwise may not have the resources to pursue," says Manzione.

David Clark, Professor and Head of MSE at Virginia Tech, believes that collaborations between universities and industry is essential. He states, "with technology making the world flatter and more competitive, we can no longer afford to work in isolation. Even if we could, we shouldn't because the greatest strides in progress come when engineers and scientists from different backgrounds work together with industry to solve problems. Providing students with the knowledge and team building skills to do this is part of our university mission."

Cary Hill, Chase Hammond and Charles Sprinkle with coated and cured guitar bodies.

By merging the resources of both schools and Taylor Guitars, "we can make better progress than any of us could individually," says Mellodge.

Expanding the Vision

Virginia Tech and the University of Hartford are seeking funding to expand this research by offering a summer program that will explore all aspects of the year-long project. The student-mentoring-student summer project will consist of five phases:

1. A visit to Taylor Guitars in El Cajon, CA to meet with their designers and tour the facility

2. A week-long program at Virginia Tech where students will utilize microwave processing hardware to produce cured wood samples and characterize them

3. A week-long program at the University of Hartford where students will perform vibrational testing on the samples produced at Virginia Tech

4. A conference where students will present the results of their work to a professional audience

5. A week-long workshop at Purdue University where the students will gain firsthand experience of the entire manufacturing process by building their own guitars

According to Folz and Mellodge, this program will provide students with the opportunity to experience the entire design process by engaging them in several weeks of intense work on different aspects of the guitar finishing project. The goal is to improve the students' understanding and broaden their perspective of engineering design and the manufacturing processes.

To learn more about how much of an impact the summer program would have on the students and the research, student and faculty travels already have begun. "We're ready for our third trip to Taylor Guitars this June, " says Folz, "and we've already started student exchanges in a limited way. The Virginia Tech team traveled to Hartford last year, and this year, the University of Hartford students and faculty spent part of their spring break at Virginia Tech. Even though we are only just beginning to assess the effects this experience has on our graduates, the ethusiasm of the project alumni speaks volumes."

On a practical level, Folz and Mellodge also hope to advance the project by having students work and make progress during the summer so that when the fall semester starts, the next group of students can pick up where the previous students left off.

Folz goes on to say, "By focusing on undergraduate research, we are able to use this collaboration as a learning tool as well as for generating new knowledge. By developing the transitional summer program, we are better preparing senior engineering students to hit the ground running after graduation, be it in industry or graduate school."

About the Authors

Katelyn Webster is a senior English major at Virginia Tech. She graduates in May 2010 with a Bachelor of Arts degree. She enjoys Hokie football and Blacksburg in the fall.

Aimee Gervacio, an English major with a concentration in Professional Writing, will be graduating from Virginia Tech with a B.A. degree in May 2010. While at Tech, she was a member of Dance Company at Virginia Tech, serving on its Executive Board in various positions, her last being Vice President. After graduation, Aimee will be pursuing a career in technical writing and editing in the northern Virginia area.

College of Engineering, Technology, and Architecture
University of Hartford

As one of seven schools and colleges that compose the University of Hartford, the College of Engineering, Technology, and Architecture (CETA) actively participates in the University's project of being "a private university with a public purpose." The undergraduate and graduate students from our departments and twelve programs all work, some beginning as early as their freshman year, on real-world projects brought to us by governments and businesses, including United Technologies Corporation and NASA.

Many of those projects come to CETA through our Engineering Applications Center (EAC) by which we partner with industry on applied research. The EAC enables regional businesses to introduce leading-edge technology and processes into their products and participate in symposia, certificate programs, and in-house training. Collaboration with industry is at the core of the practice-based nature of our curricula.

The Center for Integrated Design (CID) offers opportunities for our students beyond the classroom. Students majoring in architecture and engineering, business in the Barney School of Business, and visual communication design in the Hartford Art School, collaborate on issues brought to the CID by governments and public and private entities, including K-12 schools and other non-profits. For example, the CID investigated how to ensure that the town center of Bloomfield, a local community, remains the cultural hub.

Still another major means of participating in cross-disciplinary work arises in the Digital Health Initiative (DHI), a collaboration of CETA engineers and students with physical therapists from the College of Education, Nursing, and Health Professions (ENHP), computer scientists from the College of Arts & Sciences, and others on campus. DHI, in partnership with major health companies and healthcare providers, develop monitoring technologies and deliver cost effective healthcare to an aging population. Technologies, such as monitors that measure and report the force difference between healthy and damaged knees, will increase in importance particularly as the Boomer generation ages.

All of the projects our students work on are integrated into the curricula offered in our departments: Civil, Environmental, and Biomedical Engineering; Electrical and Computer Engineering (which includes electrical and computer engineering technology programs along with a four-year audio engineering technology program); Mechanical Engineering (which includes mechanical engineering technology and an acoustical engineering and music program that requires a musical education at the Hartt School of Music); and Architecture (which includes an engineering technology program along with the design track and one of two NAAB-accredited M.Arch programs in Connecticut, the other being at Yale University). All of the departments offer opportunities for real-world problem solving through senior capstone projects and the like.

The education we offer our students is also augmented by the various professional organizations we offer: American Institute of Architecture Students, Formula Society of Automotive Engineers, Institute of Electronic and Electrical Engineers, and many others. Such organizations give students a view beyond the classroom and help them bridge college and professional careers.

With these organizations and an outstanding and active faculty and staff, we accomplish our twin goals of educating our students and participating as a citizen in our region. For more information about CETA, EAC, CID, DHI, and our other organizations and programs, please visit our website at *uhaweb.hartford.edu/ceta*, our blog at *cetablog.blogspot.com*, or call 860.768.4446.

University of Hartford, Hawk

The South Dakota School of Mines and Technology (SDSM&T), located in Rapid City at the base of the Black Hills, offers a comprehensive spectrum of degrees focused on science and engineering. The Department of Materials and Metallurgical Engineering offers a B.S. degree in Metallurgical Engineering and M.S. and PhD degrees in Materials and Metallurgical Engineering. The undergraduate degree program has approximately 80 students enrolled. Program features include a National Science Foundation Research Experiences for Undergraduates (REU) Site called Back to the Future! As the name implies, the site focuses upon research projects that are both cutting-edge and of historical significance. For example, students conduct advanced materials research on aspects of friction stir processing as well as topics of historical significance, such as the corrosion of the USS Arizona. Students selected for the 10-week summer program come from both SDSM&T and other universities. The Back to the Future! program also includes exciting extracurricular activities associated with the beautiful Black Hills area, including day-trips to Mount Rushmore, Crazy Horse Memorial, the Badlands, and Devils Tower. For more details on this program, contact Dr. Michael West (Michael.West@sdsmt.edu), REU Site Director.

ROSE-HULMAN
INSTITUTE OF TECHNOLOGY

The mechanical engineering curriculum at Rose-Hulman Institute of Technology is designed to prepare students for productive careers in industry, government, education, and private consulting, as well as for graduate study. Thus it is based on the fundamental principles of science and engineering. These principles provide a strong foundation that enables students to apply what they have learned to the complex technological problems of today and to teach themselves the new technologies of tomorrow. The strength of the program and department consists of twenty-five faculty and four staff who serve over 550 undergraduates. These teachers provide a dynamic and innovative student learning environment to maintain and increase technical competence in a rapidly changing world. Over four years, the Institute has invested over $800,000 in improving and updating laboratory equipment and facilities. These investments contribute to the program's national recognition and number one ranking for eleven consecutive years by U.S. News & World Report for programs that offer the Bachelors or the Masters degree as the top degree in engineering. Popular competitive programs as EcoCar - the Next Challenge; Rose-Hulman Efficient Vehicle; Human Powered Vehicle; Team Rose Motor Sports; and Design, Build, and Fly, continue to stimulate interest, excitement and success throughout the department and Institute.

JUMR
Journal of Undergraduate Materials Research

JUMR Symposium at Materials Science and Technology 2009 Conference

Speakers and session chairs of the MS&T'09 JUMR Symposium

JUMR showcases undergraduate research by organizing an annual symposium at the Materials Science & Technology Conference. Sixteen undergraduate students from universities across the country presented their work at MS&T'09 (October 26, 2009, Pittsburgh, PA). Participating universities included:

- Wright State
- Virginia Tech
- Penn State
- Georgia Tech
- Miami University
- University of Central Florida
- Ohio State University
- Visvesvaraya National Institute of Technology, India
- Indian Institute of Technology, Chennai, India

The keynote speaker for MS&T'09, Dr. Daniele Finotello, Director of the NSF-DMR Office of Special Programs, emphasized the importance of higher education and research opportunities for undergraduate students. He also said, "graduate education is a long-term investment and students should seriously consider pursuing their higher education."

These symposiums are an excellent opportunity for undergraduate students to present research. JUMR looks forward to hosting another symposium at MS&T'10 in Houston, Texas.

Microwave Processing of Polymeric Coatings for Guitar Woods

Chase Hammond[1], Cary Hill[1], Charles Sprinkle[1], Andrew Sorenson[2], Stalin Vera[2]

[1]Virginia Polytechnic Institute and State University, Department of Materials Science & Engineering, Blacksburg, Virginia 24061
[2]Universtiy of Hartford, Acoustical Engineering Laboratory, Department of Mechanical Engineering, West Hartford, Connecticut 06117

Abstract

Microwave energy was used to cure polymer coatings on instrument-grade wood. A processing method was developed that included spray coating the polymer onto raw wood panels and pulling the coated panels through a 2.45GHz multi-mode microwave cavity by means of a low-power motor. Materials characterization and testing used to analyze the feasibility of using microwave processing as a coating method for guitar woods included dielectric property measurements, moisture content measurements, density measurements, and scanning electron microscopy (SEM). Also, vibrational analysis was used to compare the damping characteristics of each coating method, providing further basis for analyzing the feasibility. A comparison was conducted between samples created using the ultraviolet curing method currently used by Taylor Guitar Co. and the microwave samples generated in this study. The results demonstrate that the microwave processing of polymeric coatings for guitar woods is feasible and produces beneficial results. SEM imaging shows enhanced interaction between the polymer and wood in the microwaved samples, which may create a stronger and more durable coating. Vibration testing shows microwave processing produced comparable damping results at half the coating thickness. This decreased coating thickness may lead to a more completely cured polymer, cost savings, and reduce emission during curing.

Keywords: Microwave, Microwave Processing, Wood Dielectrics, Wood Acoustics, Polymer Coatings.

1. Introduction

Taylor Guitars currently uses an ultraviolet (UV) process to cure their protective and aesthetic polymeric coatings. Taylor Guitar Co. knows that the UV polymer they use does not completely cure during processing, meaning that the polymer may not be completely cured when it leaves their factory. This issue, coupled with their desire to increase quality control, lead to an interest in microwave energy as a means to improve on their current processing method. Microwave processing has the potential to improve upon the current UV method in a variety of ways. First, microwave energy induces significant molecular movement in the form of polarization; this phenomenon has been shown to increase the penetration of one material into another[1]. This enhanced penetration, coupled with heating due to microwave interaction with the material, could create a stronger bond between the wood and polymer. Second, microwave energy propagates with a larger wavelength than UV energy. Larger wavelengths penetrate deeper into some materials and can transfer energy further into the material[2]. This behavior could be beneficial in two ways. The deep penetration of energy could enhance molecular diffusion into the substrate material cross-section, as discussed above. In addition, deeper penetration of the microwave energy could lead to a more uniform cure of the polymer. In UV curing, a large quantity of energy may be absorbed at the surface of the polymer causing the surface to cure first.

To determine the feasibility of microwave curing, this project had three goals. First, a microwave was developed

for processing the wood provided by Taylor Guitar Co. and the polymer coating. Second, uncoated, Taylor UV-coated, and microwave-processed wood substrates were analyzed for comparison. Third, the wood's damping characteristics were analyzed and a comparison was drawn between the UV-cured and microwave-cured samples.

2. Experimental Setup and Procedure

2.1 Overview

The materials characterization performed at Virginia Tech included dielectric measurements, moisture content analysis, and density testing of the wood before processing. Dielectric characteristics (dielectric loss and dielectric constant) dictate how a material will interact with a microwave field. Materials with a higher dielectric loss will more readily heat because they have an increased ability to dissipate energy transferred to them by an electromagnetic (EM) field (dissipation is often in the form of heat). Materials with a higher dielectric constant will also allow microwave energy to penetrate deeper into the bulk and attenuate within the material, meaning the material has an increased ability to absorb microwave energy[3].

Moisture content was analyzed using thermogravimetric analysis (TGA), and the data was used to determine a temperature for drying wood samples. "Dried wood" was dried for 3-4 hours at the temperature that removed all the free water. Density of the wood was calculated using equation 1 for further understanding of the wood substrates.

$$\text{Density} = \text{Mass}/\text{Volume} \qquad (1)$$

Optical microscopy and SEM were used to observe the interaction between the wood and the polymer and to determine if there were any significant differences between UV- and microwave-processed samples. The SEM provided high magnification and high resolution images that could be used to draw conclusions about the wood/polymer interface. Along with the materials testing conducted at Virginia Tech, students at the University of Hartford conducted vibration tests to assess the acoustical quality of the microwave-processed wood. Wood substrates sent from Taylor (both UV-coated and uncoated) were compared to the wood substrates produced by Virginia Tech to determine if microwave processing had any distinct or drastic effects on the acoustic properties of the wood.

2.2 Dielectric Testing

Dielectric testing using a cavity perturbation methodwas performed on instrument-grade maple and rosewood samples provided by Taylor. This cavity perturbation technique measures a resonant cavity's frequency shift when a sample is introduced. The equations for calculating the complex permittivity (dielectric loss and constant) have been derived by F. Adams et al[4]. Adams shows that small cylindrical samples can be used to calculate the complex permittivity with less than 5% error at 2.45 GHz, and this error can be reduced by further calibration, accomplishing error values as low as 1% for low loss materials (tan (δ) <=0.3). The theory assumes that the sample is placed in a uniform field and that the radius of the sample is much smaller (approximately 5% or less) than the wavelength of the resonating EM field [4]. This measurement technique is suitable for a wide range of applications including biological materials such as wood[5].

Small cylindrical wood samples, approximately 9 millimeters long and 2.8 millimeters in diameter, were created for use in testing. Six samples of each wood species were tested. The cavity was calibrated using Teflon standards on each day measurements were taken on the wood to ensure accuracy. For clarification, "longitudinal" refers to cut wood samples with grains oriented parallel to the cylinder's axis and "transverse" refers to cut wood samples with grains oriented perpendicular to the cylinder's axis. When placed in the testing chamber, the samples were oriented so that the microwave field propagated in the direction perpendicular to the cylinder's axis.

2.2 Coating

A water-based urethane was selected as the coating for this experiment because its performance in a microwave field was most favorable based on experimental observations. Application of the coating was achieved by obtaining a compressor with a spray painting attachment. The amount of urethane deposited on the surface was controlled by adjusting the pressure settings of the compressor (~50 psi) and the speed at which the sprayer was manually passed over the wood substrates.

2.3 Air-drying of Water-based Urethane

A coated sample was allowed to cure in air for comparison with the microwave sample. Since the polymer system was not the UV-activated composition used by Taylor, a baseline comparison was needed to evaluate the effects of the microwave process, if any resulted. The manufacturer's instructions suggested the urethane could cure in air with no external influence. Each coat was allowed to dry in air (approx. 20°C) for 24 hours. There were three coats and they were sprayed using the same method discussed above.

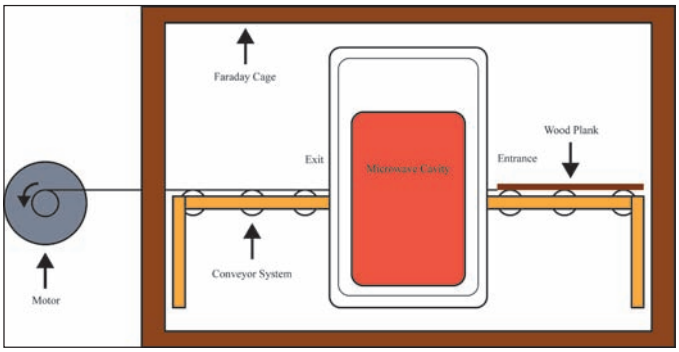

Figure 1. Schematic of complete microwave set-up. The motor can be seen on the left. The microwave with slots and the conveyor system can be seen inside the Faraday cage.

2.4 Microwave Setup

After experimentation with both single-mode and multi-mode microwave cavities, it was determined that a 2.45 GHz multi-mode cavity containing a low intensity electromagnetic field was less prone to burning the wood substrates, contained a broader field distribution allowing for processing of larger samples, and was easily controlled for this particular process. Figure 1 shows the complete microwave set-up used for wood processing. In order to accommodate large panels of wood (six inches by two feet) needed for vibrational testing, slots approximately seven inches long and one inch wide were cut in the sides of the microwave cavity. A pulley and conveyor system was developed and integrated into the microwave design. To contain leaks, a Faraday cage was constructed using wood and aluminum screen.

2.5 Microwave Processing of Maple

Based on dielectric properties, ease of machining, and availability, maple was selected as the primary species for curing experiments. Substrates machined to the correct dimensions were provided by Taylor. Each coating was sprayed manually with the compressor and spray gun to achieve as even as possible coatings. However, some human error in the thickness of the coating was expected. Four samples (6 inches by 2 feet) of maple were successfully processed.

Once the first coating was applied, the wood was attached to the motor using nylon fishing line and was pulled through the microwave at a constant speed. The total time that any part of the wood spent in the microwave was approximately two minutes; this time was chosen based on observational experimentation. After the first coat was microwave-processed; the wood was buffed using a hand-held sander and felt polishing attachments. This process significantly affected the smoothness of the polymer coating, leading to a more aesthetic appearance. Two more coats were applied and microwaved using the same method without additional buffing, resulting in a total of three coats, and an approximate thickness of 100 µm.

2.6 Scanning Electron Microscopy

Cross-sectional fracture surfaces of four different maple samples were imaged to analyze the wood/polymer interface and determine the effects that different processing techniques may have had on the composite system. The four different samples were: 1) uncoated wood, 2) UV-coated wood (prepared by Taylor), 3) air-dried wood (water-based urethane coatings allowed to cure onto the maple in air), and 4) microwaved samples (water-based urethane coatings cured using the microwave process described above). A LEO (Zeiss) 1550 high-performance Schottky field-emission SEM was used in this analysis.

2.7 Vibration Testing

Maple panels (uncoated, UV-processed, and microwave-processed) were provided to researchers at the Acoustical Engineering Laboratory at the University of Hartford. A modal analysis was conducted on each sample to determine the acoustical effects of finishes on wood. Modal analysis is a method of modeling a multi-degree of freedom system as a series of single degree of freedom mode shapes, natural frequencies and damping factors. The selection of the response point, referred to as driving point, was conducted on each sample. The panels were mapped with a rectangular grid that consisted of 40 points from which vibration data were collected. Each of the 40 test points was located with respect to the driving point and tapped with a modal impact hammer while the vibration responses were measured using an accelerometer. To ensure accurate data, the measurements consisted of a linear average of three taps whose coherence, or accuracy between all three taps, was limited to >90 % at all frequency peaks. Finally, the modes of vibration of the predominant frequencies of each sample were identified using a modal analysis program called STAR Struck. The damping factor, a measurement of vibration loss per cycle, was calculated for each of the analyzed modes. Each pair of similar samples was averaged together to account for slight differences in mass and natural differences of wood. Those results can be seen in Table 1 and a photo of the set-up for vibration testing at the University of Hartford can be seen in Figure 2.

Table 1. Damping Results for Uncoated, UV-cured, and Microwave-cured Wood Samples.

Sample	Average Mass (grams)	Average Damping (%)
Uncured	127.5	1.262
UV Cured	134	2.260
Microwave Cured	133.5	2.287

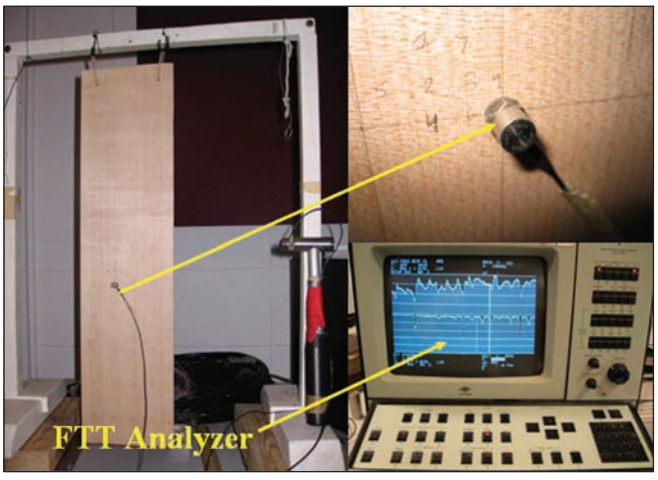

Figure 2.Vibration testing set-up at University of Hartford.

3. Results and Discussion

3.1 Dielectric Testing

The dielectric loss for as-received and dried maple can be seen in Figure 3, and the dielectric constant for the same wood samples can be seen in Figure 4.

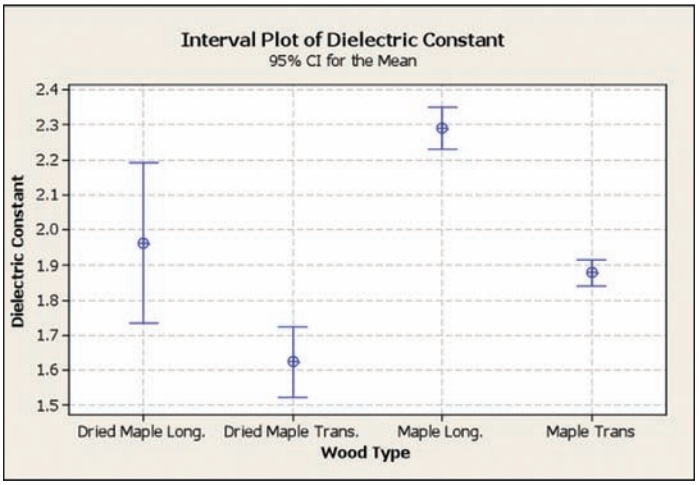

Figure 3. Dielectric constant for as-received and dried maple.

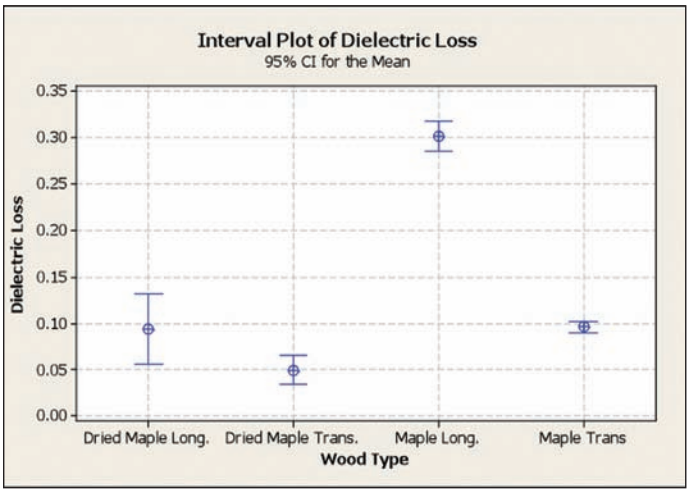

Figure 4. Dielectric loss for as-received and dried maple.

Note that the dielectric constant and dielectric loss change depending on the wood orientation with respect to the EM field. The as-received longitudinal samples showed a larger mean dielectric constant and loss of 2.29 and 0.30, respectively, than the transverse samples, which had a mean dielectric constant and loss of 1.88 and 0.098, respectively. This result implies that the microwave energy will penetrate and heat the wood more effectively in the longitudinal direction. The changes in dielectric loss and constant values due to orientation were attributed to the heterogeneous structure of the wood.

Water content also has an effect on the wood's dielectric characteristics. The dielectric loss of the wood decreases after the wood has been dried. This occurred in both the longitudinal and transverse directions. After drying the wood, the values for dielectric loss of the longitudinal and transverse samples were 0.095 and 0.050, respectively. Water has a high dielectric loss and constant; therefore, it is believed that, when the water is removed from the wood system, the loss decreases because the actual wood structure (excluding the free water trapped in the wood) has a smaller loss. It is also apparent that removing the water had a larger effect on longitudinal direction's loss than the transverse direction's loss. The change in the dielectric loss due to drying was much more dramatic for the longitudinal direction than the transverse direction.

The dielectric constant of the wood behaved similarly to the dielectric loss when the wood was dried. There was a marked decease in the values after drying. The longitudinal sample had a mean dielectric constant value of 1.96, and the transverse sample had a mean value of 1.63.

3.2 SEM Imaging

3.2.1 Uncoated Wood: Figure 5 shows an image of the raw (uncoated) wood taken at 1000X. The structure of the wood is heterogeneous, as expected. Some structural features even appear to be running perpendicular to the grain structure. The fracture surface was relatively smooth and served as a good cross-sectional area for ascertaining information about the wood/polymer interface and interaction. All SEM images of a polymer/wood interface (Figure 6-8) are shown at a 2000X magnification for comparison.

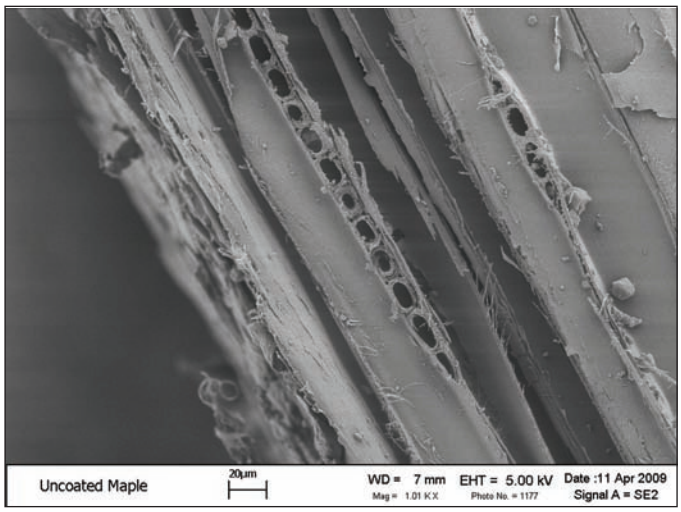

Figure 5. SEM of uncoated maple (1000X).

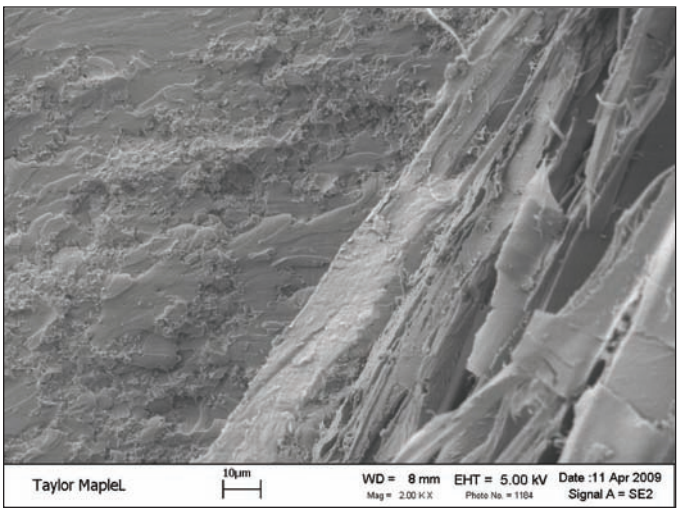

Figure 6. SEM of UV-cured, polymer-coated maple, (2000X).

3.2.2 UV-processed Wood (Taylor): Figure 6 shows maple coated with Taylor's polymer using their UV curing

method. Wood structure similar to that seen in Figure 5 was visible on the right. On the left, a darker and more homogenous polymer layer was present. The coating and wood interface was quite distinct; it appears that there was little diffusion nor interaction between the two components. This distinction could result from the fact that Taylor uses a viscous "base coat" that helps create a very smooth coating by filling in small cracks in the wood surface. The viscous layer could resist penetration into the wood. The very distinct interface (little interaction) could also be a result of the nature of UV processing. As stated earlier, larger wavelengths allow more energy to penetrate into a material. Ultraviolet rays have a relatively small wavelength (~10^{-8} m) on the electromagnetic spectrum, leading to more interaction with the surface of highly absorbing materials, thus leading to less interaction at the interface. In other words, a significant portion of the energy was consumed at the surface of the polymer leaving very little energy to help drive the polymer into the wood.

3.2.3 Air-dried Urethane Coating: The air-dried, water-based urethane coating is shown in Figure 7. This image shows a quite defined polymer/wood interface, even more so than the UV-cured sample (Figure 6). The polymer layer looks like it was very loosely bonded with the wood. Gaps between the wood and polymer can be seen at various points along the interface. It appears that the water-based urethane had limited interaction with the wood when allowed to dry in air.

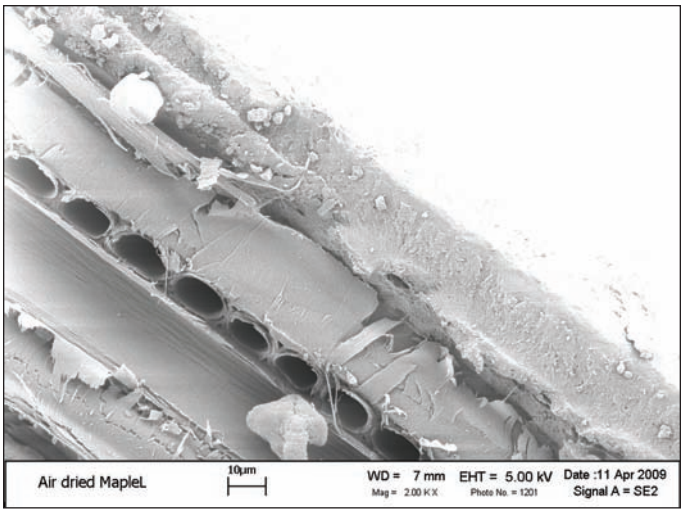

Figure 7. SEM of water-based, urethane-coated maple (air-dried) (2000X).

3.2.4 Microwave-processed Urethane Coating: Figure 8 shows a sample of maple coated with the water-based urethane cured using the designed microwave process. It is apparent that the microwave process has some effect on the interaction between the wood and the polymer. In contrast to Figures 6 and 7, the interface was much more difficult to pinpoint. A slight difference was seen between the wood and the polymer, but was much less defined than the previous images. It is believed that this characteristic is due to the high polymer/microwave interaction, resulting in a very blended composite. Microwave processing appears to drive the polymer into the wood more so than air drying and even UV curing. This difference could result from the large wavelength of microwaves (~10^{-2} m), compared with that of UV (~10^{-8} m), or from the considerable molecular movement that microwave processing induces within the water-based polymer.

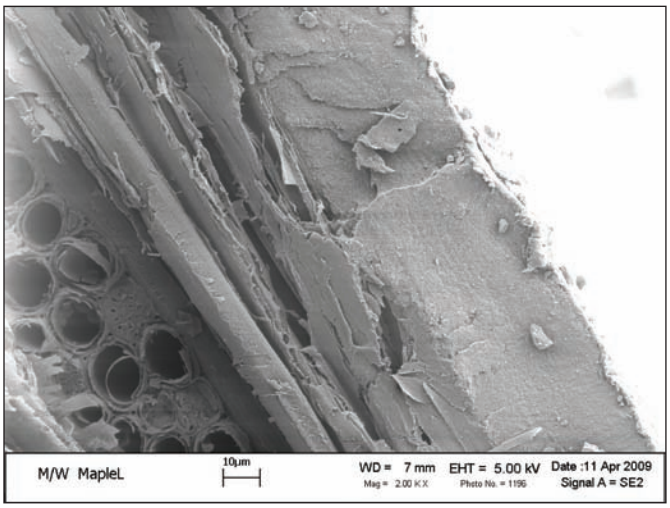

Figure 8. Water-based, urethane-coated maple (microwave-cured) (2000X).

3.3 Vibration Testing

The results indicate a 44% average increase in damping for the coated samples versus the uncoated samples. This result was expected since the finishes applied to the wood have an effect on the amplitude of oscillations that the wood undergoes while it vibrates freely. Note that while the ultraviolet coating has a greater mass than the microwave coating, the microwave samples, with only 3 coats of finish applied, have nearly the same amount of damping. Further research is required to determine the extent to which this increase in damping would affect the acoustical properties of a manufactured guitar. The amount of damping in a finished product will ultimately have an effect on a guitar's ability to resonate.

3.4 Future Work

Future work will include investigating or creating different polymers that interact more favorably with a microwave environment, analysis of the exact effects of microwave processing on the polymer and the wood, and further characterization of the wood/polymer system. Further research is required to understand the process and make in more applicable for Taylor Guitars and the guitar coating industry.

4. Conclusion

Results indicate that microwave processing of polymeric coatings for guitar woods is quite feasible. A process for coating a guitar wood substrate was successfully developed. The dielectric data could prove important in understanding the interaction of the wood with microwave

energy. Dielectric testing indicates that wood is a microwave absorber and that by manipulating the water content and orientation, the degree of absorption can be controlled.

The wood/polymer system behaved rather favorably in a microwave environment. Microwave processing appears to create a more coherent wood/polymer interface. This observation agrees with the initial hypothesis that microwaves may increase diffusion and interaction between the wood and polymer. SEM imaging shows that UV-cured and air-dried samples have a more defined interface when compared to microwave-processed samples. These results suggest microwave processing may thus be used to create adherent and strong coatings using less coating mass. Also, vibration testing results show that the average damping of the microwave-processed samples (water-based urethane coated wood) is similar to that of the UV-cured samples from Taylor. This average damping value in the microwaved samples was achieved with half the coating thickness. Decreased coating thickness (less polymer mass) may result in a more completely cured polymer. Decreased coating thickness may result in decreased cost and emissions. Therefore, it is suggested that microwave processing has the potential to improve upon Taylor's current UV process, and can have a significant effect on the processing of polymeric coatings for guitar woods.

Acknowledgements

This work was completed at Virginia Tech and University of Hartford as senior design projects. The authors would like to thank our advisors, Ms. Diane Folz, Dr. Marie Paretti, and Dr. Robert Celmer, for all their expertise in advising and overseeing this project. We would like to thank Mr. Carlos Folgar and Mr. Raghu Thridandapani at Virginia Tech for their invaluable advice and help in the laboratory, and Dr. Patricia Mellodge at Hartford for her input and insights. Finally, we would also like to thank Taylor Guitars for supplying the testing substrates, and for their expert advice regarding the guitar manufacturing environment, particularly Matt Guzzetta and Steve Baldwin.

References

[1] F. Fathi et al., "Surface modification of sodium aluminosilicate glasses using microwave energy," Ceramic Transactions, 1991, 21, 623-629.

[2] D. A. Copson, "Microwave heating," The AVI Publishing Company: Westport, Connecticut, 1962.

[3] B. G. A. McConnell, "Coupled heat transfer and electromagnetic model for simulating microwave heating of thin dielectric materials in a resonant cavity," MS thesis, Virginia Polytechnic Institute and State University, Blacksburg, VA, 1999.

[4] F. Adams et al., "Sample shape correction factors for cavity perturbation measurements," Microwave Power Electromagnetic Energy, 1992, 27, 131-135.

[5] A. Kaubaa et al., "Complex dielectric properties of the sapwood of aspen, white birch, yellow birch, and sugar maple," Drying Technology, 2008, 26, 568-578.

About the Authors

Chase Hammond graduated with a Bachelor of Science from the Department of Materials Science and Engineering at Virginia Tech in May 2009. He has accepted a job at the United States Patent Office.

Cary Hill graduated with a Bachelor of Science from the Department of Materials Science and Engineering at Virginia Tech in May 2009. He worked as a co-op student at Yokohama Tire Corporation in Salem, VA, and part-time as an intern at Luna Innovations in Blacksburg during his collegiate career.

Charles Sprinkle graduated from the Department of Materials Science and Engineering at Virginia Tech in May 2009. He has been accepted into Graduate School at Virginia Tech for a Master of Engineering degree for the 2009-2010 school year.

Andy Sorenson holds a Bachelor of Science in Engineering from the University of Hartford, where he studied acoustical engineering and jazz guitar.

Stalin L. Vera earned a Bachelor of Science in Engineering from University of Hartford, where he studied acoustical engineering and classical guitar performance.

The Dynamics of Periodically Forced Prolate Spheroids in a Quiescent Newtonian Fluid with Weak Inertia

Priyank Vijaya Kumar

Indian Institute of Technology Madras Department of Metallurgical and Materials Engineering, Chennai - 600 036, India

Abstract

The effects of convective and unsteady inertia on the dynamics of periodically forced neutrally buoyant prolate spheroids in a quiescent Newtonian fluid medium, at low Reynolds numbers have been modeled. The resulting nonlinear equations have been solved using appropriate numerical methods. Several tests including a perturbation analysis are performed to validate results. A preferred direction, which is identified as the initial direction of motion, is observed that manifests itself in the properties of the solution. Results of the behaviour of various parameters with respect to the Reynolds number, aspect ratio of the spheroid and the amplitude of the periodic force are presented. The results are technologically important as they may lead to insights in the development of active dampeners and smart fluids.

Keywords: Low Reynolds Number, Quiescent Fluid, Prolate Spheroid, Aspect Ratio, Periodic Force, Inertial Effects

1. Introduction

Suspensions of solid particles are encountered both as raw materials and as intermediates in a large number of industries such as printing and paper making, petroleum, pharmaceuticals, and food processing. Suspension rheology leads to insights which may lead to better control of fluid stress deformation behaviour and hence may lead to appropriate changes in processing parameters. In most situations, the particles tend to be non-spherical or even irregularly shaped, the suspension rheology then being sensitive to the orientation distribution of the suspended particles. The motion of non-spherical particles in shear flows at vanishingly small Reynolds numbers has been studied theoretically for a long time and is summarized by Leal[1]. It has, in fact been known since the work of Jeffery[2] and later Bretherton[3] at zero Reynolds numbers, that in the absence of inertia, an axisymmetric particle in a simple shear flow rotates periodically in one of an infinite single–parameter family of closed 'Jeffery' orbits. The particular orbit adopted by the particle, in the absence of hydrodynamic interactions, Brownian motion, etc. depends on the initial conditions, rendering the inertialess limit indeterminate. Subramanian and Koch[4] considered both particle and fluid inertia as a possible mechanism acting to remove this indeterminancy. They developed solutions for aspect ratios close to unity. Hence, their analysis captures the leading order effect of the deviation from sphericity on the particle orientational motion. They found that for the neutrally buoyant case, the inertia of the suspending fluid causes a prolate spheroid to drift toward an axial spin about the vorticity axis of the ambient simple shear.

Ramamohan and coworkers[5,6] have been studying the dynamics and rheology of periodically forced suspensions for a period of about two decades. The class of problems they have studied has fundamental importance and technological potential. This class of problems is one of the simplest physically realizable fluid dynamical systems that can show chaos at the level of the individual particle. It has been shown that there exists a chaotic parametric regime, in the dynamics of periodically forced spheroidal particles in a simple shear flow[7]. This chaotic dynamics can be controlled by controlling the system parameters[8]. These results restricted to zero Reynolds numbers and simple shear flow have been summarized by Asokan et al[5].

Recently Ramamohan et al[6], have studied the dynamics and rheology of a dilute suspension of neutrally buoyant periodically forced spherical particles in a quiescent Newtonian fluid at low Reynolds numbers. Since most realistic suspensions have non-spherical shapes, The results reported in this work show that data based on simulations with spheres may need to be modified before they can be

applied to realistic situations. Hence, in this paper, these results are extended to prolate spheroidal particle suspensions.

Table 1. List of Symbols.

F^H	Hydrodynamic force on particle
F_s^H	Steady force drag on particle
F^{Ext}	External force on particle
Φ	Stokes resistance tensor
M	Transformation tensor defined such that $u_0=MU_s$
U_s	Slip velocity of the particle
U^∞	Velocity of the fluid
U_p	Velocity of the particle
Y_s	Displacement of the particle
Re	Reynolds number
Sl	Strouhal number
U_C	Characteristic velocity of the particle
F_0	Amplitude of the periodic force
Re_F	Scaled amplitude of the periodic force
ω	Frequency of oscillation
a	Characteristic particle dimension, semi-major axis of the spheroid
b	Semi-minor axis of the spheroid
e	Eccentricity of the spheroid
m_p	Mass of the particle
ρ	Density of the particle
ν	Kinematic viscosity of the fluid
μ	Viscosity of the fluid
Y_{pmean}	Mean displacement of the particle

2. The Hydrodynamic Force Expression for an Arbitrary Shaped Particle

Lovalenti and Brady[9] give the expression for the required hydrodynamic force on an arbitrary shaped particle, in the long time limit at low Reynolds numbers.

This is the most rigorous equation which results in an ODE at low but non-zero Re. The reciprocal theorem has been used to obtain the following expression. The details of the derivation can be found in Lovalenti and Brady[9].

$$\boldsymbol{F}^H(t) = ReSlV_P\dot{\boldsymbol{U}}^\infty(t) + \boldsymbol{F}_S^H(t) - ReSl\left[6\pi\boldsymbol{\phi}.\boldsymbol{\phi}.\boldsymbol{\phi} + \lim_{R\to\infty}\left(\int_{V_F(R)}\boldsymbol{M}^T.\boldsymbol{M}dV - \frac{9\pi}{2}\boldsymbol{\phi}.\boldsymbol{\phi}R\right)\right].\dot{\boldsymbol{U}}_S(t) + \frac{3}{8}\left(\frac{ReSl}{\pi}\right)^{\frac{1}{2}}\left\{\int_{-\infty}^{t}\left[\frac{2}{3}\boldsymbol{F}_S^{H\parallel}(t) - \left\{\frac{1}{|A|^2}\left(\frac{\pi^{\frac{1}{2}}}{2|A|}\mathrm{erf}(|A|) - \exp(-|A|^2)\right)\right\}\boldsymbol{F}_S^{H\parallel}(s) + \frac{2}{3}\boldsymbol{F}_S^{H\perp}(t) - \left\{\exp(-|A|^2) - \frac{1}{2|A|^2}\left(\frac{\pi^{\frac{1}{2}}}{2|A|}\mathrm{erf}(|A|) - \exp(-|A|^2)\right)\right\}\boldsymbol{F}_S^{H\perp}(s)\right] \times \frac{2ds}{(t-s)^{1/2}}\right\}.\boldsymbol{\phi} - Re\lim_{R\to\infty}\int_{V_F(R)}(\boldsymbol{u}_0.\nabla\boldsymbol{u}_0 - \boldsymbol{U}_s(t).\nabla\boldsymbol{u}_0).\boldsymbol{M} + O(ReSl) + O(Re) \quad (1)$$

Here, $\boldsymbol{U}_s = \boldsymbol{U}_p - \boldsymbol{U}^\infty$ is the slip velocity of the particle. $\boldsymbol{U}_p$ is the velocity of the particle. $\boldsymbol{U}_s$ has been non-dimensionalized by $\boldsymbol{U}_c$. The acceleration terms $\dot{\boldsymbol{U}}_S$ and $\dot{\boldsymbol{U}}^\infty$ are non- dimensionalized by $\omega\boldsymbol{U}_c$, where $1/\omega$ is the characteristic timescale. $\boldsymbol{U}^\infty$ is the velocity of the fluid as $r\to\infty$. *Re* is the Reynolds number, defined as $Re=U_ca/\nu$ based on a characteristic particle slip velocity, $\boldsymbol{U}_c$, '*a*' denotes the characteristic particle dimension, in this case the semi-major axis and ν is the kinematic viscosity of the fluid. $\boldsymbol{F}_S^H = -6\pi(\boldsymbol{\phi}.\boldsymbol{U}_S)$, $\boldsymbol{F}_S^{H\parallel} = -6\pi(\boldsymbol{\phi}.\boldsymbol{U}_S).(\boldsymbol{pp})$, $\boldsymbol{F}_S^{H\perp} = -6\pi(\boldsymbol{\phi}.\boldsymbol{U}_S).(\boldsymbol{\delta}-\boldsymbol{pp})$, where $\boldsymbol{\delta}$ is the idem tensor of order 2 and unit vector $\boldsymbol{p} = \frac{\boldsymbol{Y}_S(t)-\boldsymbol{Y}_S(s)}{|\boldsymbol{Y}_S(t)-\boldsymbol{Y}_S(s)|}$, here $\boldsymbol{Y}_s(t)$-$\boldsymbol{Y}_s(s)$ is the integrated displacement of the particle relative to the fluid from time *s* to the current time *t*. $\boldsymbol{F}^H$ is scaled by $\mu a\boldsymbol{U}_c$. *Sl* is the Strouhal number, V_P is the scaled particle volume and '*A*' is given by

$$A = \frac{Re}{2}\left(\frac{t-s}{ReSl}\right)^{\frac{1}{2}}\left(\frac{\boldsymbol{Y}_S(t)-\boldsymbol{Y}_S(t)}{t-s}\right)$$

The first term on the right hand side of the differential expression is due to an accelerating reference frame. The second is the pseudo-steady Stokes drag. The third is called the acceleration reaction, similar to the added mass. The fourth term represents the unsteady Oseen correction, which replaces the 'Basset memory integral' in the long time limit at finite Reynolds number. The last integral contributes a lift force, i.e. a force perpendicular to the slip velocity. Note that the expression is valid up to order *Re* and order *ReSl*.

The acceleration reaction term (I_1=int-xx in Table-2) is computed using the expressions given by Pozrikidis[10] and

Chwang and Hu[11]. The expression for the Stokes resistance tensor (Φ) in its dimensionless form is given by

$$\boldsymbol{\phi} = \frac{8e}{3}(\boldsymbol{a}) \qquad (2)$$

Here, e is the eccentricity of the spheroid and a is the diagonal matrix mentioned in Chwang and Hu[11].

Table 2. Computed Values of the Diagonal Matrix Representing the Acceleration Reaction Term.

Aspect Ratio (a/b)	int-xx	int-yy	int-zz
2	0.7261	1.3266	1.3897
3	0.3510	0.7915	0.8378
4	0.2288	0.5447	0.5828
5	0.1624	0.3963	0.4292
6	0.1242	0.3009	0.3301
7	0.0998	0.2353	0.2619
8	0.0830	0.1872	0.2124
9	0.0682	0.1487	0.1723
10	0.0591	0.1208	0.1430

In the current work, only one dimensional motion of the particle is considered. The translation is along this major axis of the spheroid and hence is symmetric with respect to the particle. The lift force term is neglected as it contributes only to a force in the perpendicular direction and is zero in this case. This has been verified in these computations.

3. Solving The Differential Equation

After obtaining suitable expressions and values for different aspect ratios, the dynamics of a spheroidal particle were determined.

3.1 Formulation of the Problem

The force equation (1) given by Lovalenti and Brady for an arbitrary shaped particle undergoing an arbitrary time-dependent motion at low Reynolds numbers, in the long time limit is considered. In this case a neutrally buoyant prolate spheroid in an infinite body of quiescent fluid is considered, as well as the effects of an external periodic force acting on the spheroid along the x-axis.

The governing expression for the unidirectional motion of a spheroid in a quiescent fluid medium is obtained, starting with zero velocity at time $t=0$, with $\boldsymbol{U}_s = \boldsymbol{U}_P - \boldsymbol{U}^{\infty}$ where $\boldsymbol{U}_p$ is the velocity of the particle, scaled with respect to the size of the particle and the frequency of the external periodic force, ω, i.e. we take $\boldsymbol{U}_c = a\omega$ and $\boldsymbol{U}^{\infty} = 0$.

Note that there exists a singularity (point at which the intergral term becomes indeterminate) at $s=t$. Hence, in order to avoid this singularity, the integral in the interval $[0, t-\epsilon]$ is evaluated, where ϵ is chosen to be a very small number. Note that in the limit $s \to t$, the integral converges to a finite limit and hence the value of the integral in the range $s=t-\epsilon$ to $s=t$ is negligible. Under these conditions, equation (1) reduces to

$$\boldsymbol{F}^H(t) = -6\pi(cof)\boldsymbol{U}_P(t) - ReSl(I_1)\dot{\boldsymbol{U}}_s(t) + \frac{3}{8}\left(\frac{ReSl}{\pi}\right)^{\frac{1}{2}}(cof)^2\left\{\int_0^{t-\epsilon}\left\{\frac{1}{|A|^2}\left(\frac{\pi^{\frac{1}{2}}}{2|A|}\mathrm{erf}(|A|) - \exp(-|A|^2)\right)\right\}\frac{12\pi\boldsymbol{U}_P(s)}{(t-s)^{3/2}}ds + 16\pi\boldsymbol{U}_P(t)\left[\frac{1}{\sqrt{t}} - \frac{1}{\sqrt{\epsilon}}\right]\right\} \qquad (3)$$

Here, $cof = \frac{8}{3}ea_{11}$ and I_1 is the computed acceleration term.

Now, the equation of motion for a neutrally buoyant particle immersed in a liquid is given by

$$\frac{m_P\dot{\boldsymbol{U}}_P(t)}{\mu a^2\omega} = \boldsymbol{F}^{ext}(t) + \boldsymbol{F}^H(t) \qquad (4)$$

The periodic force $\boldsymbol{F}^{ext}(t) = \boldsymbol{F}_0\sin(t)$ is used, where time has been scaled with respect to the frequency of the external periodic force. The following equations for the displacement and velocity of the particle using Newtons second law of motion were obtained.

$$\frac{d\boldsymbol{Y}_P}{dt} = \boldsymbol{U}_P \qquad (5)$$

$$\frac{d\boldsymbol{U}_P}{dt} = \frac{1}{Re'}\left[Re_F\sin(t) - 6\pi(cof)\boldsymbol{U}_P + \frac{3}{8}\left(\frac{ReSl}{\pi}\right)^{\frac{1}{2}}(cof)^2(P_1 + Q_1)\right] \qquad (6)$$

where,

$$Re' = \frac{4\pi}{3}\left(\frac{b}{a}\right)^2 Re + (I_1)ReSl\,,\quad Re_F = \frac{F_0}{\mu a^2\omega}\,,\quad Re = \frac{\rho a^2\omega}{\mu}$$

Here, a is the characteristic particle dimension, ρ is the density of the particle and μ is the fluid viscosity.

$$P_1 = \int_0^{t-\epsilon}\left\{\frac{1}{|A|^2}\left(\frac{\pi^{\frac{1}{2}}}{2|A|}\mathrm{erf}(|A|) - \exp(-|A|^2)\right)\right\}\frac{12\pi U_P(s)}{(t-s)^{3/2}}ds$$

$$Q_1 = 16\pi\boldsymbol{U}_P(t)\left[\frac{1}{\sqrt{t}} - \frac{1}{\sqrt{\epsilon}}\right]$$

3.2 Numerical Procedure

The differential equation was solved using a time-stepping finite difference routine. In order to accommodate the nonlinear integral term, the product trapezoidal rule[12] was implemented. The value of ε was chosen to be equal to 0.0001. Further decrease in its value did not result in any significant changes of the velocity and displacement values.

Two sets of data points, 150000 and 350000, taken at an interval of 0.0001 in both the dimensionless velocity and dimensionless position were generated. Further increase in resolution did not yield any significant difference in the results.

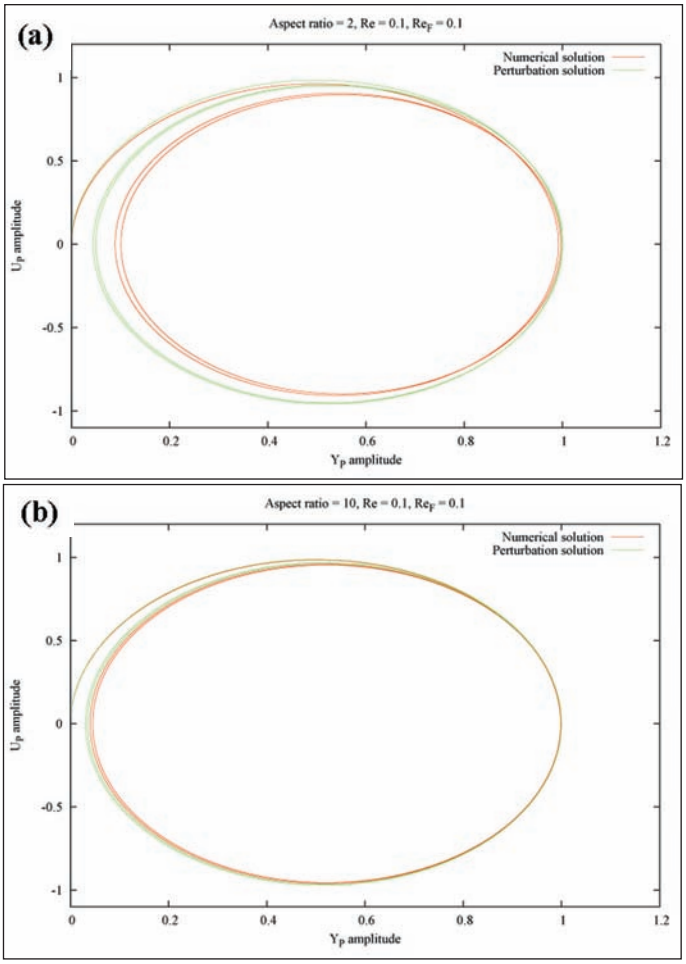

Figure 1. The phase plot obtained compares the numerical solution with the perturbed solution. This has been seen for Re=0.1, ReF=0.1, aspect ratio=2(a) and 10(b). The match is very good in the second case owing to reduced inertial effects at higher aspect ratios and hence reduced nonlinearity.

3.3 Tests

Several tests were performed in order to validate the results. They are listed below.

3.3.1 Test 1 Perturbation Analysis

Perturbation solutions were obtained in order to validate our results for small Re. The Taylor series expansion for the nonlinear integral term was used. One important aspect to be noted is that the expression given for an arbitrary shaped particle (prolate spheroid in our case) is correct upto O(ReSl).

The perturbation parameter was chosen to be Reynolds number, Re. The hydrodynamic force expression for an arbitrary shaped particle given by Lovalenti and Brady is valid up to O(Re).

Hence, the perturbed solution upto O(Re) was expressed as follows

$$U_P = U_0 + U_1 Re^{1/2} + U_2 Re + O(Re)$$

where,

$$U_0 = \frac{Re_F \sin(t)}{6\pi(cof)}$$

$$U_1 = \frac{QU_0}{6\pi(cof)}\left[\frac{1}{\sqrt{t}} - \frac{1}{\sqrt{\epsilon}}\right] + \frac{3Re_F(Sl\pi)^{1/2}}{(6\pi)^2}\int_0^{t-\epsilon}\frac{\sin(s)}{(t-s)^{3/2}}ds$$

$$U_2 = \frac{-1}{6\pi(cof)}\left\{\frac{c_1 Re_F \cos(t)}{6\pi(cof)} - QU_1\left[\frac{1}{\sqrt{t}} - \frac{1}{\sqrt{\epsilon}}\right] - 3(Sl\pi)^{1/2}(cof)^2\int_0^{t-\epsilon}\frac{U_1(s)}{(t-s)^{3/2}}ds\right\}$$

wherein $Q = 6(Sl\pi)^{1/2}(cof)^2$, $c_1 = \frac{4\pi}{3}\left(\frac{b}{a}\right)^2 + (I_1)Sl$.

The displacement is calculated by numerically integrating the interpolated data of the velocity.

MATLAB was used for computing the above expressions. We found that for low values of Re, typically upto Re=0.2, both the perturbed and the numerical solutions agreed well. Figure 1 shows a comparison between the phase plots obtained by both the methods for aspect ratios 2 and 10, Re=0.1 and ReF = 0.1.

3.3.2 Test 2

When the initial direction of the motion was reversed, namely by replacing ReF with – ReF , the phase space plot was reflected about the zero velocity axis. That is, a reflection of the phase space attractor about the zero velocity axis when the direction of the first motion is reversed was obtained, which can be considered as an important result which demonstrates the correctness of the results.

The results showed a preferred direction in the solution. Since the only physical direction in this problem is the initial direction of the external force, a reversal of that direction should result in a reversal of direction in the solution, which was indeed the case. The tests performed above provide considerable confidence in the results.

4. Results and Discussion

We have four variable parameters in the system; the Reynolds number Re, the Strouhal number Sl, the aspect ratio and the amplitude of the periodic force ReF. It is essential to determine the effect of these parameters on the system. Typical phase space plots (plots of particle velocity vs. position) have been generated for different values

of the Reynolds number, the aspect ratio and the amplitude of the periodic force. In some of the Figures (Figure 3b and Figure 5c), the displacement and velocity values were scaled with their appropriate maximum values obtained in the Stokes' case, i.e. when Re = 0. These values have been termed as displacement and velocity amplitude, respectively. This illuminates the results better so that the individual cases can be compared. One of the parameters was chosen, namely the Strouhal number, a constant and equal to unity. The plots represent an attractor as they are bounded in phase space. Since Sl always occurs in combination with Re, the limit of small Sl number is automatically obtained by reducing Re.

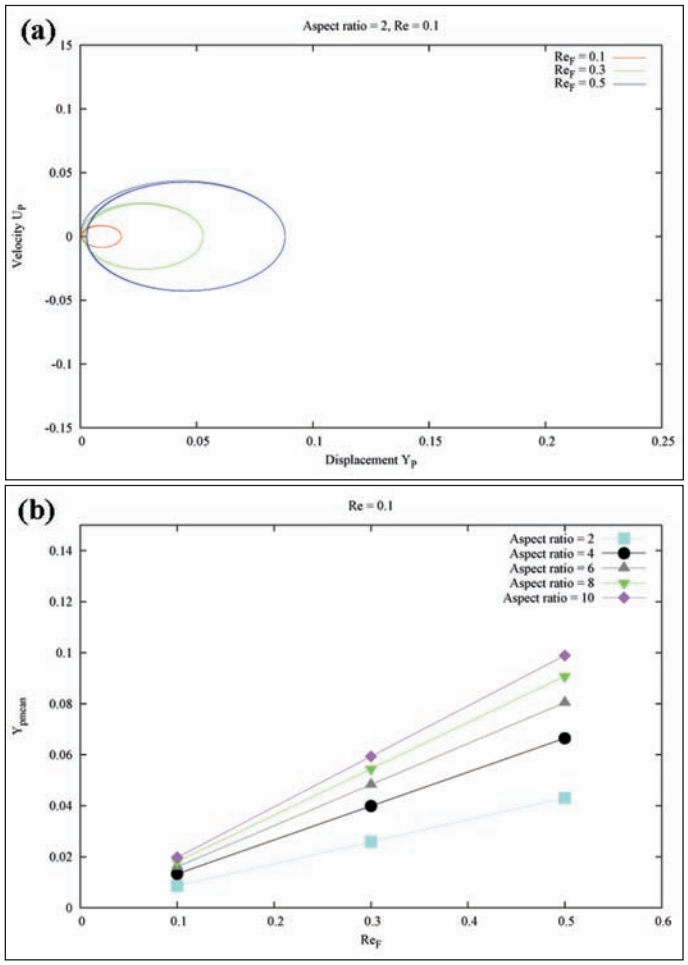

Figure 2. (a) This phase portrait shows the effect of ReF on the system. On increasing the value of ReF, the phase plots get enlarged showing the obvious effect of the forcing term. The phase plots for different ReF values (0.1, 0.3, 0.5), Re=0.1, aspect ratio=2 are superimposed. (b) Plot showing the relationship of Ypmean with ReF.

It was observed that the particle tends to move away from the zero displacement axis with time, i.e. after every cycle, we notice that the mean position is shifted along the displacement axis. This is termed as drift. The average displacement of the particle is determined from the zero-velocity axis and is denoted as Y_{pmean} . There exists a definite relation between Y_{pmean} and Re, as well as Y_{pmean} and Re_F .

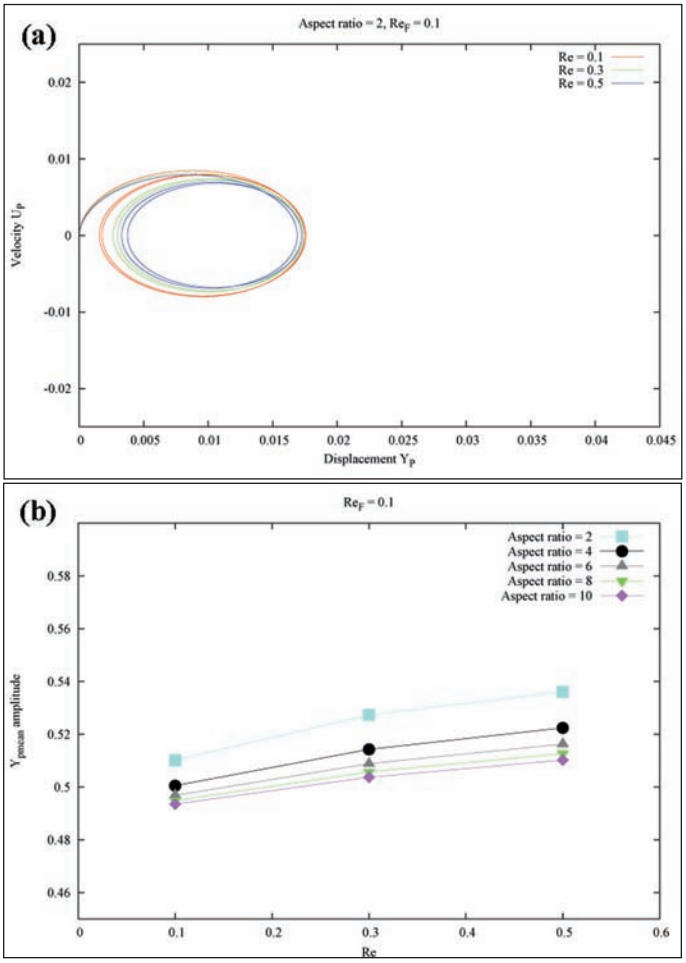

Figure 3. (a) Phase portrait obtained for different Re values (0.1, 0.3, 0.5), ReF=0.1, aspect ratio=2. We can see the effect of increasing Re which results in diminished phase plots. (b) Plot showing the relationship of Ypmean amplitude with Re.

4.1 Effect of Re_F

The area bounded by the phase space plot which is bounded and hence represents an attractor in phase space, increases with increasing amplitude of the forcing term, ReF, establishing the obvious relation between the attractors and the amplitude of the periodic force. As ReF increases, the particle oscillates with larger amplitude and thus covers a larger surface area in the phase plot. As can be seen from the Figure 2(a), the increase in area is quite significant when ReF is increased from 0.1 to 0.5.

4.2 Effect of Re

The effect of increasing the Reynolds number can be seen from Figure 3(a). The effect is opposite compared to that of increasing the amplitude of the forcing term. Increasing Re results in a smaller attractor plot. This shows the effect of inertia on the motion of the particle. Inertial effects dominate at higher Reynolds number and the mean

position of the particle is seen to shift in the direction of initial motion on increasing Re.

4.3 Effect of Aspect Ratio

The values obtained for the acceleration reaction term for different aspect ratios are given in Table 2. The values of the second and third diagonal elements of the tensor are quite similar to one another. This is expected as they both are symmetric to the direction of motion of particle, in the current work. These values provide an idea about the reaction to particle motion and hence the term acceleration reaction. As can be seen, the values decrease with increasing aspect ratio. These values appear in the term Re' in the equation (6). This term additionally contains a factor which is the square of the inverse of aspect ratio. Hence, the effect of this term decreases with increasing aspect ratio. The contribution from the Pseudo-steady Stokes drag also decreases with increasing aspect ratio which again contributes to lower resistance. The lowering of resistance with aspect ratio could be due to the body becoming more streamlined and hence being able to move through the fluid medium easily. Thus, the overall effect of increasing aspect ratio can be seen as an increase in the area bounded by the attractor. The effect of aspect ratio on Y_{pmean} was studied and it was found that Y_{pmean} increases with aspect ratio. This result can be seen in Figure 4.

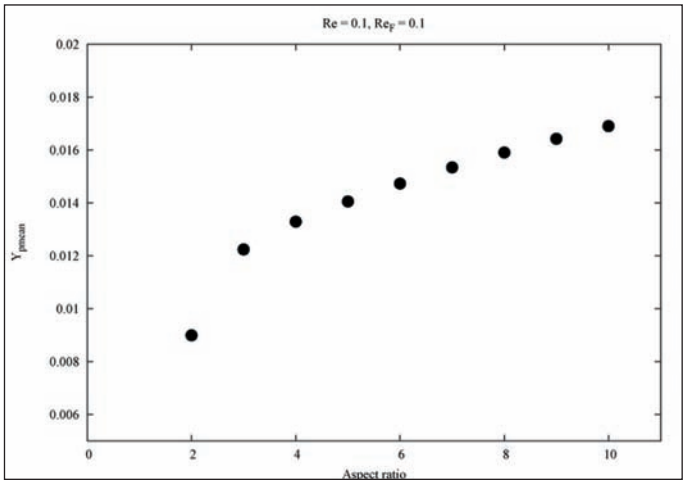

Figure 4. Plot showing the relationship of Ypmean with aspect ratio.

4.4 Effect of Inertia on Steady State

In order to determine the influence of the inertial effects with every cycle, the simulation was run for longer times, typically about 350000 iterations. The phase plots obtained are presented in Figure 5(a,b).

It can be seen that in the initial cycles, the drift is significant when compared to the drift in the later stages of the simulation. Thus, we see that the inertial effects are dominant during the initial stages and later on the particle tends towards an oscillatory steady state. We observe that the inertial effects dominate at lower aspect ratios and their dominance reduces with increasing aspect ratio.

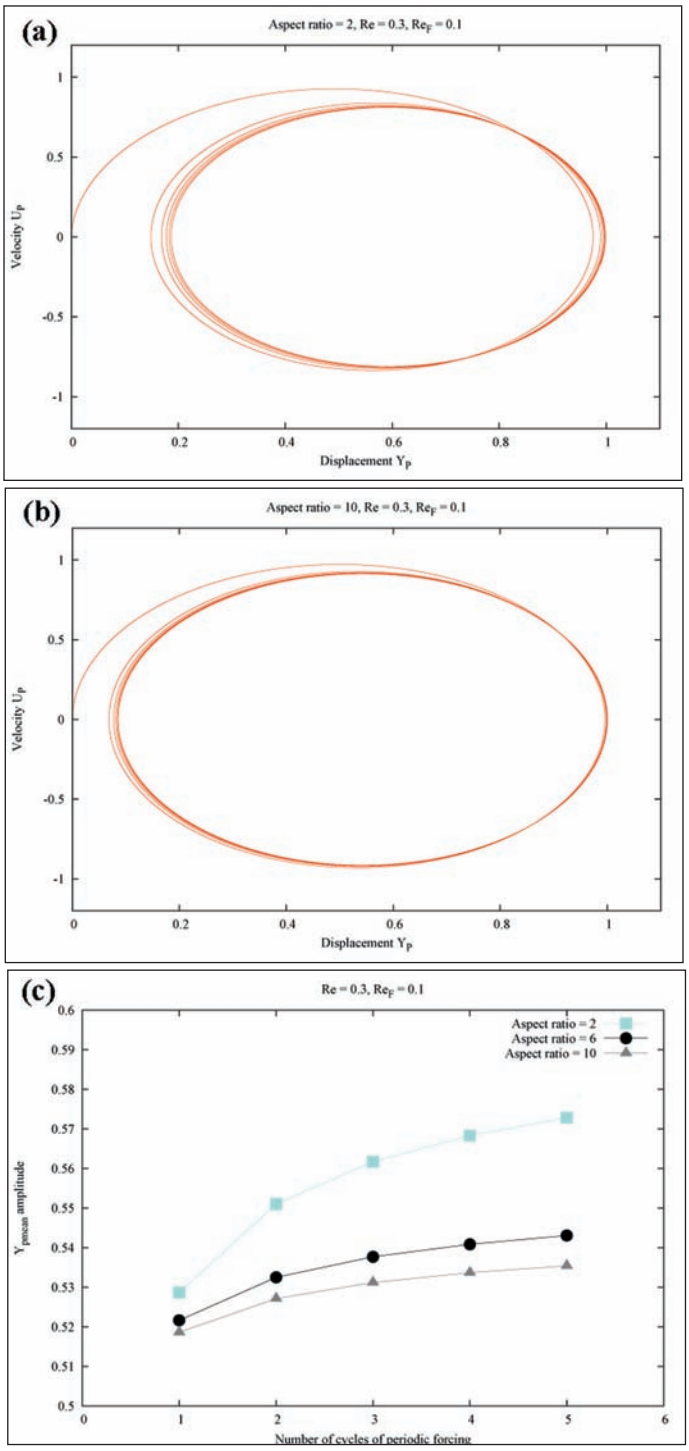

Figure 5. The phase plots obtained for aspect ratio=2 (a) and 10 (b), Re=0.3, ReF=0.1, showing the long time inertial effects and attainment of the steady state. The attainment of the steady state is quicker in (b) as the inertial effects die down quickly due to their relatively insignificant contribution at higher aspect ratios (c) plot showing the drift in mean position with every complete cycle of periodic forcing. Note that the particle attains a steady mean position at longer times.

The attainment of an oscillatory steady state is found to be quicker when the aspect ratio is larger. This happens due to weaker inertial effects. Figure 5(c) shows this effect clearly. Here, we scale Y_{pmean} obtained after every cycle of the periodic forcing term with respect to the maximum displacement obtained in Stokes' case. A steady value of this Y_{pmean} amplitude is attained more quickly when aspect ratio increases.

4.5 Effect of Nonlinearity

The behaviour of the system was analysed by neglecting the unsteady Oseen correction term which contains the non-linear term and compared it with the attractors obtained from the full differential expression (Figure 6).

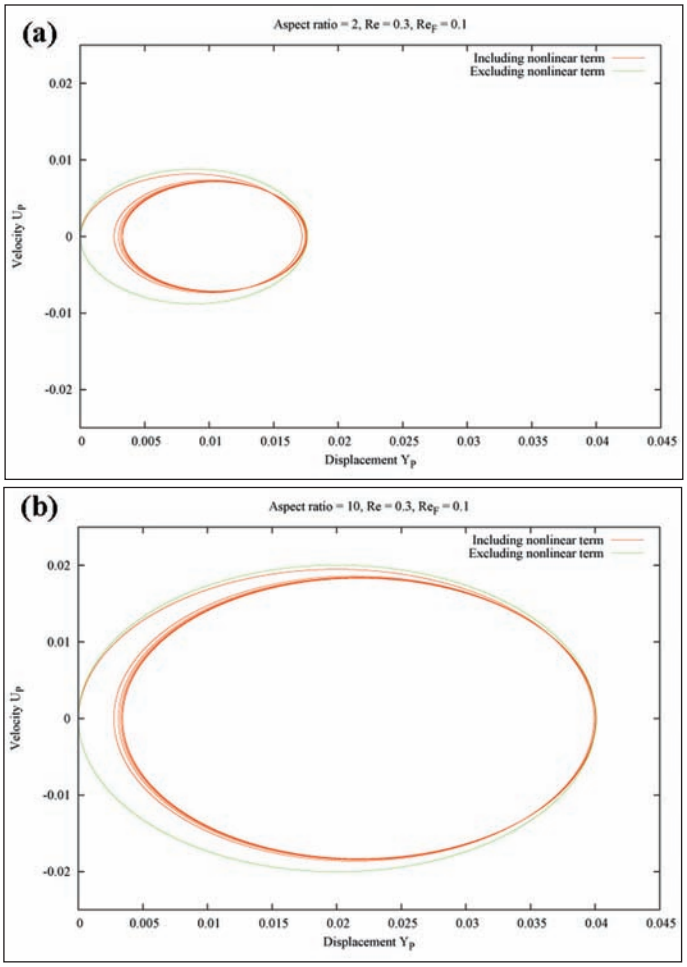

Figure 6. The phase portrait comparing the plots obtained with and without the inclusion of the Oseen correction term and thereby the non-linear term. The effect of inertia on the system can be clearly seen. The non-linear term contribution at higher aspect ratio is reduced and we can see it approaching the curve obtained by neglecting the non-linear term. Here, Re=0.3, ReF=0.1, aspect ratio=2 (a) and 10 (b).

From this, the effects of the non-linear and inertial terms are clear. The phase plots excluding the Oseen correction cover a larger surface area. Another important observation is the absence of drift of the particle from the zero velocity axis. The particle is found to oscillate about a single point. The attainment of steady state is thus strongly dependent on inertia. A slight variation in the parameters considered could vary the inertia and thus approach to steady state.

5. Conclusion

In this paper, an attempt has been made to determine the dynamics of a prolate spheroid under periodic forcing in a quiescent Newtonian fluid medium at low Reynolds numbers. Inertial effects have been included to study the behaviour more realistically. The numerical values for the acceleration reaction term for different aspect ratios were presented. It is observed that these values decrease with increasing aspect ratio.

1. The particle is seen to oscillate under periodic forcing. A preferred direction of motion is observed and it is seen that the particle shows a net displacement along this direction with time.

2. The effect of system variables is studied in detail and it is found that increasing Re restricts the particle motion and hence the size of the attractor.

3. Increasing the periodic force amplitude is found to increase the size of the attractor.

4. The effect of the shape of the particle is studied by varying the aspect ratio. The size of the attractor increases with increasing aspect ratio due to weaker inertial effects.

The results were supplimented with detailed physical arguments and wherever possible, various tests have been conducted to justify the results. The ultimate goal is the rheology, which can be further obtained using the results in this paper, since this will determine the stress deformation behaviour and will determine processing parameters for these suspensions. It is hoped that this work excites further research in this area. Future work could possibly cover 2-D and 3-D aspects of such a motion. It would also be interesting to study the effects of coupling rotation with translation.

Acknowledgements

This work was done at Centre for Mathematical Modelling and Computer Simulation, Bangalore, India, as a part of B.Tech internship. The author would like to acknowledge Dr. T. R. Ramamohan for his continuous guidance. He would like to thank K. Madhukar and Prof. I. S. Shivakumara for their encouragement and Dr. A. R. Upadhya, for his help in taking up this project at National Aerospace Laboratories, Bangalore.

References

[1] L. G. Leal, "Particle motions in a viscous fluid," Annual Reviews in Fluid Mechanics, 1980, 12, 435-476.

[2] G. B. Jeffery, "The motion of ellipsoidal particles immersed in a viscous fluid," Proceedings of the Royal Society of London A, 1922, 102, 161-179.

[3] F. P. Bretherton, "The motion of rigid particles in a shear flow at low Reynolds numbers," Journal of Fluid Mechanics, 1962, 14, 284-304.

[4] G. Subramanian et al., "Inertial effects on the orientation of nearly spherical particles in simple shear flow," 2006, 557, 257-296.

[5] K. Asokan et al., "Review of chaos in the dynamics and rheology of suspensions of orientable particles in simple shear flow subjected to an external periodic force," Journal of Non-Newtonian Fluid Mechanics, 2005, 129, 128-142.

[6] T. R. Ramamohan et al., "Numerical Simulation of the Dynamics of a Periodically Forced Spherical Particle in a Quiescent Newtonian Fluid at Low Reynolds Numbers, Lecture Notes on Computational Science, 2009, 5544, 591-600.

[7] C. V. A. Kumar et al., "Chaotic dynamics of periodically forced spheroids in simple shear flow with potential application to particle separation," Rheologic Acta, 1995, 34, 504-512.

[8] C. V. A. Kumar et al., "Controlling chaotic dynamics of periodically forced spheroids in simple shear flow: results for an example of a potential application," Sadhana, 1998, 23, 131-149.

[9] P. M. Lovalenti et al., "The hydrodynamic force on a rigid particle undergoing arbitrary timedependent motion at small Reynolds number," Journal of Fluid Mechanics, 1993, 256, 561-605.

[10] C. Pozrikidis, "Boundary integral and singularity methods for linearized viscous flow," Cambridge University Press, 1992.

[11] A. T. Chwang et al., "Hydromechanics of low-Reynolds-number flow. Part 2. Singularity method for Stokes flows," Journal of Fluid Mechanics, 1975, 67, 787-815.

[12] T. Tang, "A finite difference scheme for partial integro-differential equations with a weakly singular kernel," Applied Numerical Mathematics, 1993, 11 ,309-319.

[13] G. K. Batchelor, "The stress system in a suspension of force free particles," Journal of Fluid Mechanics, 1970, 41, 545-570.

[14] P. M. Kulkarni et al., "Suspension properties at finite reynolds numbers from simulated shear flow," Physics Fluids, 2008, 20, 040602.

[15] K. Sangtae and S. J. Karrila, "Microhydrodynamics, principles and selected applications," Dover Publications Inc., Mineola, New York, 2005.

[16] Introduction to Perturbation Method, Web link: http://www.sm.luth.se/~tomas/applmath/chap2en/index.html

[17] A. H. Nayfeh, "Perturbation Methods," Wiley Interscience Publication, 1973.

[18] Gradshteyn and Ryzhik, "Table of Integrals," Series and Products, Academic, New York, 1965.

[19] J. D. Lambert, "Computational Methods in Ordinary Differential Equations," Wiley Interscience Publication, 1973.

About the Author

Priyank V. Kumar is an undergraduate student of Metallurgical and Materials engineering at Indian Institute of Technology-Madras, Chennai, India. He joined the department in the month of August, 2006 and is expected to graduate in May 2010. His research interests include Computational Material Sciences, Transport phenomena, Mechanical Metallurgy and Thermodynamics. He has been working on specific topics such as Inertial effects on forced particles at low Reynolds numbers, Molecular Dynamics simulation of Ni/NiAl interfaces, Micromechanical simulation of wear resistant coatings and Computational modelling of Electron Beam Welding process. He has carried out his internship at CSIR Centre for Mathematical modelling and Computer Simulation, Bangalore, India (Summer and Winter '08) and was awarded the DAAD scholarship for his research intern at Institut fur Materialprufung Werkstoffkunde und Festigkeitslehre, University of Stuttgart, Germany (Summer '09). His hobbies include playing cricket, drumming and listening to music.

Gamma Ray Scintillators via BaF_2:Ce Nanopowders

M. Brooke Barta

Georgia Tech Research Institute, Georgia Institute of Technology, Atlanta, Georgia 30332

Abstract

Nano-scale BaF_2:Ce phosphor powders ("nanophosphors") show great potential for improving the functioning of inorganic scintillators for gamma ray detectors. These particles may offer greater efficiency and ease of manufacture than most state-of-the-art single crystal scintillators currently in use. Chemical precipitation similar to that of LaF_3: Ce synthesis was used to prepare the BaF_2:Ce powders, while care was taken to optimize doping levels to prevent internal absorption while maximizing photon production. Select particle samples were then encapsulated in a polymer matrix in an attempt to improve mechanical robustness while maintaining photon yield. Results from photoluminescence excitation and emission measurements of samples of BaF_2: Ce powders doped from 1-30mol% suggest that the BaF_2:15mol%Ce sample exhibited the greatest photon production, but that a more UV transparent polymer must be found in order to maximize light transmission when the powder is encapsulated in a polymer matrix.

Keywords: Nanophosphor Synthesis, Characterization

1. Introduction

1.1 Motivation for Development

According to the Security and Accountability for Every Port Act (SAFE Port Act, H.R. 4954), all cargo entering the country must be scanned for threatening radioactive material[1]. Current scintillator detectors are fragile, hygroscopic, and unable to classify the specific isotope emitting radiation. This research focuses on improving two main scintillator properties: photon yield and bulk density[2]. Photon yield/production refers to the number of photons produced per MeV of gamma ray energy absorbed,[3] while bulk density correlates to the atomic weight of the host/dopant material. Ideal scintillators will have a light yield of more than 5×104 photons/MeV, and high bulk density (alkaline/actinide elements) for increased photon interaction[3].

The best scintillators currently in use are single crystals of NaI, doped with less than 1mol% Tl. These scintillators have a photon yield of 4.1×10^4 photons/MeV and a density[2] of 3.67 g/cm^3. NaI(Tl) single crystals can be grown easily and economically, but are extremely fragile and hygroscopic, and so must be encased in a protective shell[3]. Large single crystals of BaF_2 have lower photon yields than NaI(Tl) crystals due to a higher concentration of defects arising from more sensitive crystal growth.[3] Difficulty arises from the need to grow large single crystals of BaF_2, but if crystal size could be decreased, photon yield and energy resolution could increase.

1.2 Inorganic Phosphor Nanopowders

Nano-scale phosphor powders (nanophosphors) offer improved photon yields compared to single crystals by minimizing absorption and scattering due to impurities, which are a problem in large crystal growth[4,5]. BaF_2:Ce nanophosphors in particular exhibit properties that suggest superior performance in scintillator technology. Energy deposited into the powder by lower energy radiation will not excite electrons in BaF_2, and thus the powder will only generate scintillation photons in the presence of high energy gamma-rays, thereby eliminating much noise from the energy spectrum[6].

1.3 Direction of Work

This investigation seeks to improve scintillators by increasing scintillation material density, and increasing photon yield by decreasing defect concentration. Past studies have indicated that scintillator efficiency can be improved by doping a host crystal with rare earth elements[3]. Maintaining this assumption, BaF_2:Ce nanopowders will be synthesized using a method similar to the chemical precipitation synthesis[7] of LaF_3:Ce. Goals include the creation of a nanophosphor with a high bulk density and increased photon production. Photoluminescence excitation (PLE) and emission (PL), and X-ray diffraction (XRD) measurements will be used to characterize all powders synthesized. Powders with high efficiency indicated by PL measurements will be encapsulated in a UV curable polymer, and

gamma ray measurements conducted to measure efficiency upon excitation by a radionuclide source. The results will be compared to single crystal NaI(Tl) scintillators, which are currently the most efficient.

2. Procedure

2.1 BaF_2:Ce Nanophosphor Synthesis

BaF_2:Ce with doping levels from 1-30mol% were synthesized. The molar amount of $Ba(NO_3)_2$ powder was held at a constant 18.89mmol while the amount of $Ce(NO_3)_3$ powder was varied from 0.2-8.09mmol to achieve the desired doping level. These powders were mixed in 80mL of deionized (DI) water in a round bottomed flask, and the mixture stirred mechanically. In a separate flask, 1.6g NaF was mixed into 100mL of DI water with a solution of 3.6g of oleic acid in 100mL of ethanol. This solution was heated to 78°C using a heating mantle. The $Ba(NO_3)_2$ solution was then added drop-wise under a nitrogen gas purge to the NaF solution, and the final mixture held and stirred at 78°C for one hour. The solution was then centrifuged at 3000 rpm for 15 minutes, then the liquid decanted and 200mL of ethanol added to each flask. The BaF_2:Ce powders were mechanically agitated and a sample of the suspension was taken and placed into a scintillation vial for photoluminescence tests. The powder was then dried in air overnight.

2.2 BaF_2:Ce Nanophosphor Characterization

Photoluminescence excitation (PLE) measurements were conducted using a Cary Eclipse Fluorescence Spectrometer with a monitor wavelength of 353nm to find the optimal excitation wavelength for the BaF_2:Ce powders. The sample was excited with wavelengths ranging from 200nm to 340nm. Photoluminescence emission (PL) measurements were conducted using a 288nm excitation beam (determined from the PLE measurements) scanning a wavelength range from 300nm to 480nm.

Transmission electron microscopy (TEM) was used to confirm that the nanophosphors were composed of individual particles, while X-ray diffraction (XRD) was used to determine BaF_2:Ce crystallite size. TEM analysis was conducted using a JEOL 100CX TEM operating at 100kV. Particle size analysis was conducted with an X'Pert Pro α-1 diffractometer equipped with a Cu Kα X-ray tube emitting at 1.54Å scanning a 2θ range from 20-70°.

2.3 Scintillator Fabrication

To match the refractive indices (RI) of the powder and polymer matrix, commercially available liquids with known RI at 589nm from Cargille Labs Inc. (Cedar Grove, NJ) were used in conjunction with a Leica M165C optical microscope and a 400nm LED. Two drops of RI matching liquid were added to 10mg of BaF_2:Ce powder on a glass slide. An optical microscope was used to determine the visibility of the powder agglomerates under each RI liquid, which was the criterion for determining the RI of the powder. After a matching liquid was found, a dispersion curve for the specific liquid was acquired from the manufacturer, and the RI of the powder estimated via a polynomial fit to the data.

A UV curable (OptiClad) polymer with a RI of 1.485 at 389nm was acquired from Ovation Polymers (Medina, OH) and used to encapsulate the BaF_2:Ce nanophosphors. The custom made polymer was a mixture of several different monomers that imparted the specific physical and optical properties needed for this investigation. BaF_2:Ce was placed into 10mL of the OptiClad polymer in a standard 40mm diameter by 30mm deep mold. The suspension was homogenized using a Fisher Scientific 550 sonic dismembrator probe to disperse the powder uniformly in the polymer, and then cured using a Lesco Rocket Cure SuperSpot Mk II UV lamp operating with a 100W DC mercury vapor short-arc.

2.4 Gamma Ray Measurements

Gamma ray measurements were conducted using a radionuclide source placed on top of the cylindrical scintillator sample. The sample and source were placed on a photomultiplier tube (PMT) and the entire apparatus encased in a shield to block excess light. Photons generated by the scintillator-gamma-ray interactions were recorded by the PMT, and assigned a "channel number" ranging from 1-12keV depending on the energy of the photon emitted. In this test, 1040 channels between 1keV and 12keV were used, with a total counting time of 6×10^4s.

3. Results and Discussion

3.1 BaF_2:Ce Synthesis

The total mass of the finished BaF_2:Ce powder was kept below 5g because it was found that extensive agglomeration would occur when the batch size exceeded 8g. Drying the finished powder in air also introduced error because BaF_2 is hygroscopic, causing the powder to absorb moisture during the drying process. This was problematic during encapsulation, when excess moisture had an adverse effect on the polymer curing process; and therefore, data collected.

3.2 PL and PLE Trends

PLE data monitored at 353nm (see Figures 1 and 2), yielded a peak at 288nm, indicating that this wavelength would most efficiently excite the BaF_2:Ce powders. A wavelength of 353nm was chosen for PLE measurements from peak locations in a PL spectra.

After the optimal 288nm excitation wavelength was determined, PL scans were conducted on samples of each doping concentration. It was found that the BaF_2:15% Ce powder sample showed the greatest light intensity between 300-480nm. Reduced photon production (concentration quenching) occurred at 15mol% Ce doping, a much higher level than in large crystals (usually less than 1mol%). One possible explanation for this discrepancy is that energy transfer may be regulated to the nanometer region, thus

the energy loss due to dopant-dopant transitions is less widespread; therefore, less serious of a problem[8].

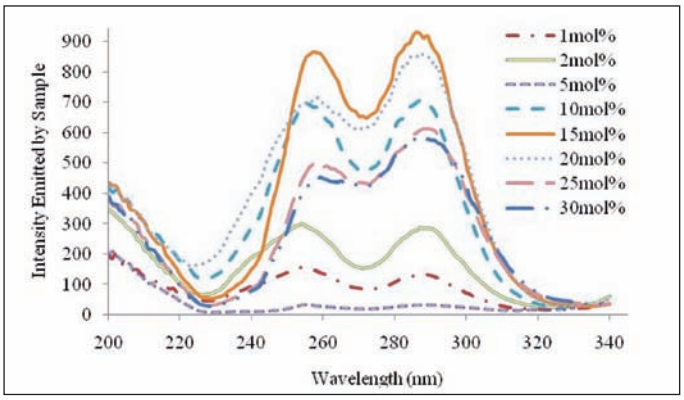

Figure 1. PLE data (l=353nm) for BaF_2:Ce powders with dopant levels 1-30mol% (see legend).

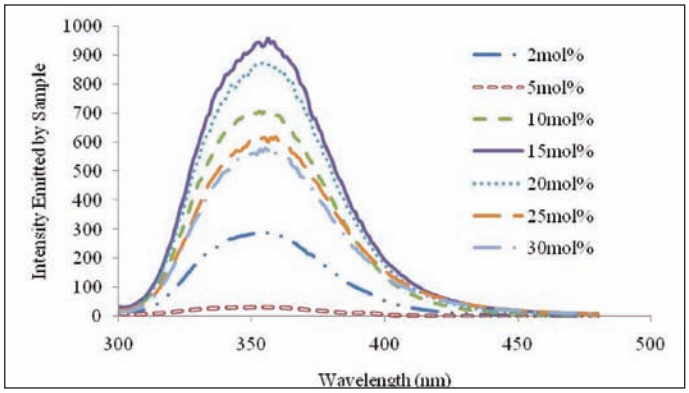

Figure 2. PL data (l=288nm) for BaF_2:Ce powders with dopant levels 1-30mol% (see legend).

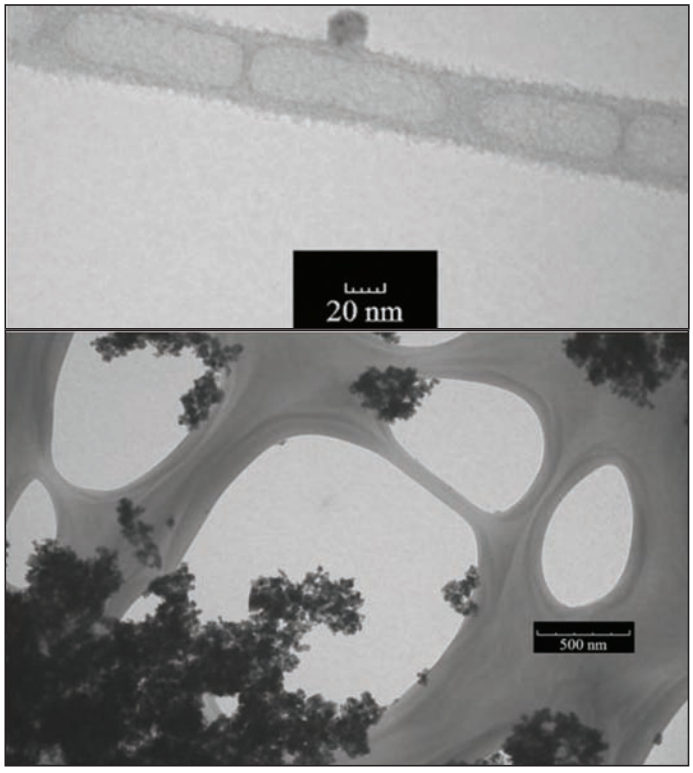

Figure 3. TEM images of BaF_2:15%Ce particle.

Via TEM observation (see Figure 3), it was concluded that the powder synthesized was composed of individual particles. Results from the XRD analysis are shown in Figure 4, and particle size was estimated to be between 40nm and 50nm using Debeye-Scherrer analysis.

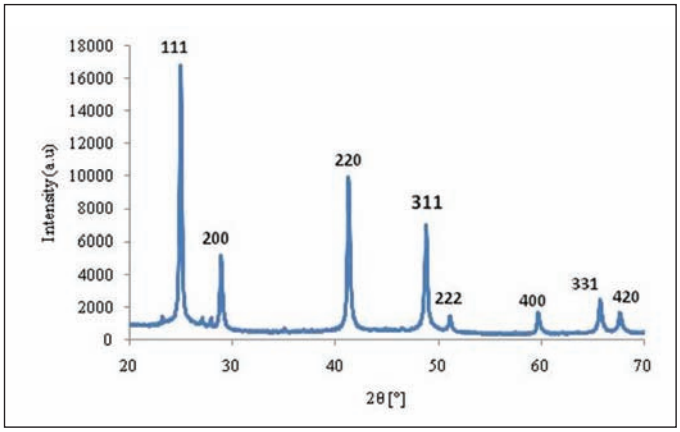

Figure 4. XRD pattern of BaF_2:1%Ce nanophosphor powder.

3.3 Nanopowder/Polymer Composite

Using RI matching liquids, it was found that the BaF_2:Ce powder should have a RI of 1.485 at 389nm. The puck of BaF_2:Ce encapsulated in the OptiClad polymer was exposed to an Am-241 radionuclide source. The counts for each channel number were summed and normalized to counting time to generate an energy spectrum (Figure 5) from photons generated by gamma-ray excitation of the phosphors.

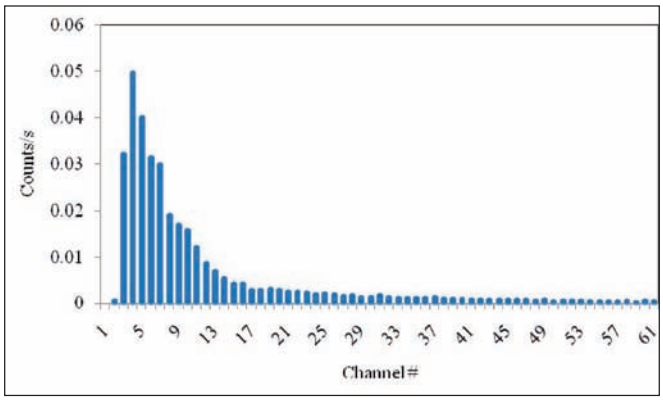

Figure 5. Gamma ray data (energy spectrum) generated by BaF_2:Ce encapsulated in UV curable matrix (50vol% solids loading), measured over 6×10^4s under an Am-241 radionuclide source.

These values would ideally generate energy peaks characteristic of Am-241, which is more accurately shown in the energy spectrum produced by a NaI(Tl) single crystal scintillator (Figure 6). It is theorized that the low photon production and poor energy resolution were caused by adverse polymer-phosphor chemical interactions, which induced photon scattering rather than transmission, causing the puck to appear a cloudy shade of yellow instead of the desired clear[9]. The opacity may also have been caused by overheating during the polymerization process, which

is exothermic, thus creating difficulty in stabilizing the sample temperature as polymer thickness increased. The high and unstable temperatures may have caused monomer burn off, thus altering the optical properties of the cured polymer. The overheating problem could be solved by placing the mold in an ice bath during curing, or chilling the sample in a refrigerator or freezer prior to curing.

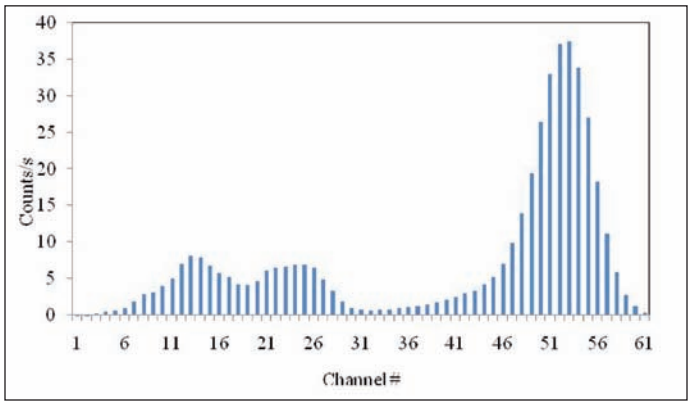

Figure 6. Gamma-ray data (energy spectrum) generated by NaI(Tl) single crystal, measured over 6×104s under an Am-241 radionuclide source.

Low resolution in the energy spectrum may also be due to a lower density of scintillating material in the composite scintillator compared to a single crystal, thus resulting in a lower light yield. The NaI(Tl) single crystal is composed entirely of scintillating material, whereas the composite scintillator was only loaded with 50vol% scintillating particles, reducing the probability of incident gamma-rays striking and interacting with scintillating material. This problem could be mitigated by encapsulating a higher concentration of particles, or pressing a pellet of BaF_2:Ce particles and using the polymer as a binder. Although 1024 channels were available during the scans, no relevant peaks were generated above channel #61, and so channels above this value are are omitted from the spectra. Removing the superfluous channels simplified analysis of the peaks that were generated by the scintillators under Am-241 excitation.

4. Conclusion

While BaF_2:15mol%Ce showed the greatest efficiency of the powders synthesized, if polymer encapsulation remains the preferred method of fabricating the nanophosphor scintillators, a polymer with a more controllable polymerization process will need to be procured. Alternatively, particles may be pressed into a pellet and the polymer used as a protective binder rather than an encapsulant in order to maximize density of scintillating material.

Future Work

Future work in nanophosphor synthesis will include doping BaF_2 with other lanthanide series ions such as Eu^{2+} that have the potential to further increase photon production. Doping with this ion is desirable because it exhibits greater fluorescence on the blue side of the light spectrum, allowing the light to pass through the polymer matrix (which absorbs light close to UV energy).

Acknowledgements

The author gratefully acknowledges Dr. Jason H. Nadler and Dr. Zhitao Kang of the Georgia Tech Research Institute at the Georgia Institute of Technology for their supervision and guidance. Research was conducted as part of an initiative by the Domestic Nuclear Detection Office (DNDO) in response to the SAFE Port Act.

References

[1] U.S. Congress, "Security and accountability for every port act,".Washington D.C, 2006.

[2] C.W.E. Van Eijk, "Inorganic-scintillator Development," Nuclear Instruments and Methods Physics Research Section A, 2001, 460, 1-14.

[3] K.W. Kramer, "Development and characterization of highly efficient new cerium doped rare earth halide scintillator materials," Journal of Materials Chemistry, 2006, 16, 2773.

[4] W. H. Tait, "Radiation Detection;" Butterworth: Boston, 1980.

[5] D. W. Cook, "Luminescent properties and reduced dimensional behavior of hydrothermally prepared Y_2SiO_5:Ce nanophosphors," Applied Physics Letters, 2006, 88, 103.

[6] A. V. Golovin, "Mechanism of short-wavelength luminescence of barium fluoride," Optics and Spectroscopy, 1988, 65, 102.

[7] J. del-Castillo, "Wide colour gamut generated in triply lanthanide doped sol-gel nano-glass-ceramics," Journal of Nanoparticles Research, 2009, 789-884.

[8] T. C. Madden, "The use of semiconductors doped with isoelectronic traps in scintillation counting," IEEE Transactions Nuclear Science, 1968, 15, 47-57.

[9] R. Rosson, personal communication, Georgia Tech Research Institute, Atlanta, GA, 2009.

About the Author

Brooke Barta is a fourth year undergraduate student majoring in Materials Science & Engineering at the Georgia Institute of Technology. She has been working at the Georgia Tech Research Institute since May 2008. After graduation in May 2010, she hopes to pursue a master's degree in the same field.

Variations in Hardness and Grain Size with Density for Fully Stabilized Zirconia Sintered Using Microwave Processing

Andrew Kulp

Virginia Polytechnic Institute and State University, Department of Materials Science & Engineering, Blacksburg, Virginia 24061

Abstract

Densification of ceramic materials with microwave energy is being considered as an alternative means to conventional methods. Using microwave processing for sintering ceramics, many researchers have observed higher densities at lower temperatures, as compared with conventional sintering methods. Microwave sintering technology is under investigation for fabricating inert matrix materials that would recycle fuel in proposed Generation IV nuclear reactors. This study examined the variation in hardness with density and the changes in microstructure with processing technique and temperature. The 8 mol% Y_2O_3-ZrO_2 samples selected for this study were sintered using a conventional furnace, a multi-mode microwave furnace and a single-mode microwave furnace. Microstructural results on 96% theoretically dense samples showed differences in grain size to processing technique (conventional = 1.58 μm, multi-mode microwave = 1.29 μm, and single-mode microwave = 8.86 μm). Vickers hardness tests were performed on select sample groups representative of each processing method. Similarly, dense samples sintered with a conventional furnace yielded a hardness of 5.37 GPa. Whereas, higher hardness values were observed in similarly dense samples that were processed in a multi-mode microwave (9.28 GPa) and single-mode microwave (7.77 GPa). The results obtained in this study favor microwave sintering at low temperature that could eventually find an application in fabricating inert matrix fuels for next generation reactors.

Keywords: Zirconia, Microwave Processing, Hardness

1. Introduction

Inert matrix fuels are being developed to recycle the spent nuclear fuel in the proposed Generation IV nuclear reactors[1-3]. These newly developed reactors will use the spent nuclear fuel, which is a byproduct of existing reactors. The problem with the radioactive materials in spent nuclear fuel (more formally known as transuranic nuclides) is that they are volatile at high temperatures (1600 °C). This behavior will result in material loss when using high temperature conventional processing. Microwave processing is being explored to fabricate these fuels at lower temperatures[4].

Extensive research has been done to determine the materials that are best suited for use as an inert matrix[5]. The materials must achieve a minimum strength (20-30 GPa) to withstand the high pressures experienced by a fuel pellet during its normal operation. They must also maintain a minimum percentage of residual porosity to contain the daughter products of the fission reaction. The ideal densification to satisfy these parameters is 85-95% theoretical density. Apart from hardness, structure (grain size) plays an important role in releasing the fission gasses that are a byproduct of a nuclear reaction[6]. Stabilized zirconia is a candidate material that has been found to have the necessary traits for this application[5].

The objective of this work is to study the hardness achieved in samples that have been processed in a conventional furnace and the two different microwave furnaces. Also, another objective is to observe the microstructural differences seen as a result of the different processing techniques.

2. Experimental Procedure

2.1 Materials and Preparation

Pellets of 8 mol % Yttria-Zirconia (8YZ) were formed using a combination of uniaxial and isostatic pressing. Sintering was performed in a conventional furnace and two different microwave furnaces (multi-mode microwave (MMM) and a single-mode microwave (SMM)). Microwave sintering results showed higher percent theoretical densities at lower temperatures[7]. A theoretical density value of 8YZ powders used in this study was estimated by R. R. Thridandapani et al. to be 5.96 g/cc (this value was obtained from the X-ray diffraction patterns).

Samples were sectioned from sintered pellets of 8YZ. The population consisted of samples processed at different temperatures (1100, 1200, 1300, 1400, and 1500 °C).

A ¼ inch wide sample was cut from the center of each pellet. This section of the pellet was chosen because it allowed more area for hardness testing to be conducted on each sample. They were then mounted, ground and polished to prepare them for hardness testing. Silicon carbide pads with grit sizes of 180, 240, 320, 400, 600 and 1000 were used for grinding. Polishing was done on felt pads using 15, 6, 3, and 1 micron diamond polishing suspension.

2.2 Vickers Hardness

Indentations were created using a Vickers micro indenter at a force of 9.8 N for a dwell time of 5 seconds. Figure 1 shows a typical view of a Vickers indentation.

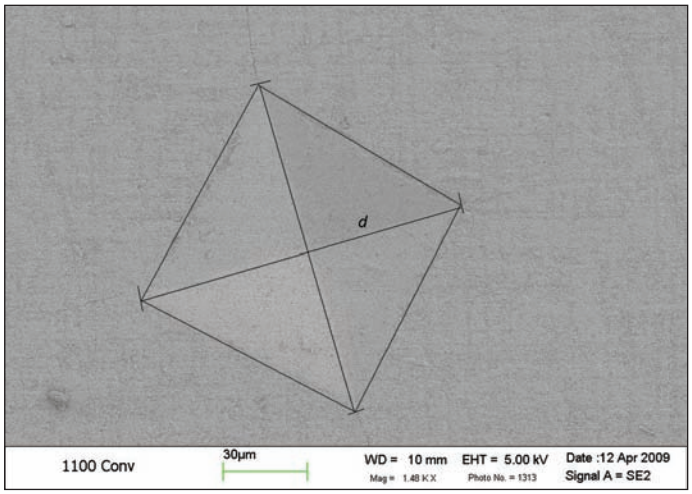

Figure 1. An example of a Vickers indentation (outlined in black).

The tests were conducted according to ASTM C 1327 standards and hardness values were calculated using equation 1.

$$HV = 0.0018544\ P/d^2 \qquad (1)$$

Where HV is the Vickers hardness value, P is the indenter load in newtons, and d is the length of the diagonal in millimeters[6].

2.3 Determination of Grain Size

For this study, the most easily measured microstructural feature is grain size. After gathering hardness data, each sample was prepared for Scanning Electron Microscopy (SEM) through thermal etching. During hardness testing, the surface of the sample must be highly polished. Therefore, due to the necessary surface etching, the SEM micrographs must be taken after the hardness testing is completed. SEM micrographs were taken for several samples from each temperature and sintering method.

Grain size measurements were conducted using the intercept method according to ASTM standards E 112. The average grain diameter was calculated using equation 2.

$$\bar{I} = L_T/N_i \qquad (2)$$

Where $\bar{I}$ is the "mean lineal intercept," which can be interpreted as the average grain diameter of the sample in µm, L_T is the test line length in µm, and N_i is the number of intercepts per test line[9].

3. Results and Discussion

3.1 Variations in Hardness with Density

As the density of the samples of 8YZ increased to approximately 96% theoretically dense, the Vickers hardness increased as well. For 96% theoretically dense specimen, the processing technique used (Conventional Furnace, MMM, or SMM) did not show a significant difference between hardness values. Figure 2 illustrates these points for the 8YZ samples processed using a conventional furnace, a multi-mode microwave furnace and a single-mode microwave furnace.

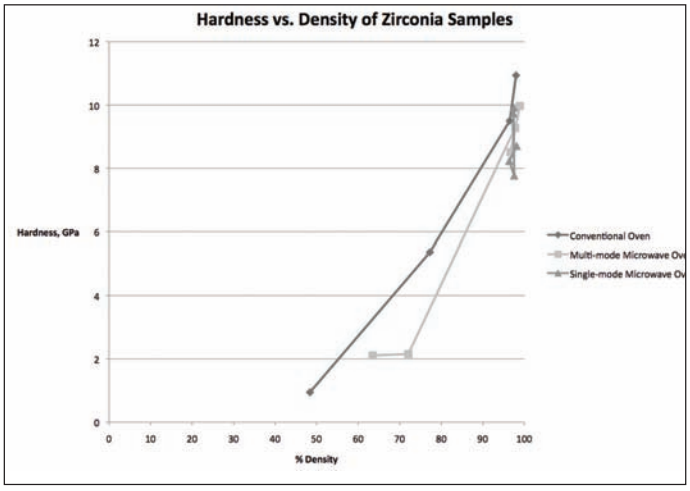

Figure 2. A plot of hardness vs. percent theoretical density for 8YZ.

3.2 Variations in Grain Size with Sintering Temperature

The samples sintered at 1100° and 1200° C using a conventional furnace and a MMM furnace did not reach full density. The microstructure of these samples showed no significant differences between each other.

All other samples were at least 96% theoretically dense, except the sample sintered at 1300 °C processed using the conventional method. This sample had a density of about 77% theoretical. The variation in sintering temperature with grain size is shown in Figure 3. It can be observed that grain size increased as the sintering temperature increased.

The data represented in Figure 3 also shows that the samples sintered using a single-mode microwave experienced a significant increase in grain size with temperature. It has been reported by many researchers that the diffusion is enhanced due to the presence of microwave energy[10]. The observed increase in grain size may be due to this improved diffusion occurring in the SMM sintering process.

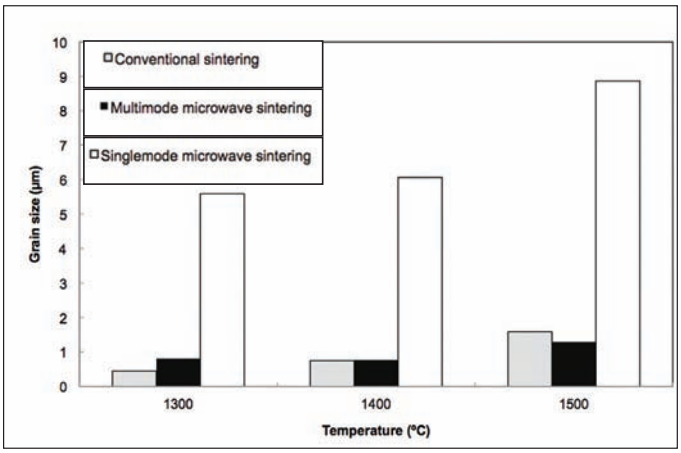

Figure 3. A bar chart of the grain size at different processing temperatures for 8YZ samples.

The micrograph images in Figure 4 show the grains and their boundaries that exist for fully dense samples of 8YZ sintered using the three different methods. An important point to notice is the similarity between the conventionally sintered and the MMM sintered samples. It can also be observed that SMM sintered samples showed a larger grain size than those produced using the other two processing techniques.

4. Conclusions

In conclusion, the hardness values showed a significant increase with percent theoretical density. The results also showed that higher hardness was achieved at lower temperatures in a microwave furnace, indicating that this method could be useful for fabricating inert matrix fuels at lower temperatures with less material loss without compromising hardness.

It was observed that the SMM samples showed a significant increase in grain size with temperature when compared with samples processed using a conventional furnace and a MMM at the same temperature. The result implies that nuclear fuels which demand larger grain size could be processed at much lower temperatures in a SMM furnace.

Acknowledgements

The author acknowledges Diane C. Folz for her guidance in this project and Raghu Thridandapani for help with conducting the experiments. He also acknowledges the Department of Energy for their financial support in conducting this research under contract number DE-FC07-05-ID14654 .

References

[1] R. J. M. Konings et al., "Fuels and targets for transmutation,"Applied Physics, 2002, 3, 1013.
[2] V. Artisyuk et al., "Challenge of transmutation of long-lived nuclides,"Progress in Nuclear.Energy, 2005, 47, 327.
[3] C. Degueldre et al., "Concepts for an inert matrix fuel," Journal of Nuclear Materials, 1999, 274,.1.
[4] K. Une et al., "Rim structure formation and high burnup fuel behavior of large-grained UO2 fuels," Journal of Nuclear Materials, 2000, 278, 54.
[5] International Atomic Energy Agency, "Viability of inert matrix fuel in reducing plutonium amounts in reactors," IAEA-TECDOC-1516, 2006.
[6] R. R. Thridandapani et al., "Microwave sintering of 8 mol % yttria-zirconia (8YZ): An inert matrix material for nuclear fuel applications," Journal of Nuclear Materials, 2009, 384, 153.
[7] M. Burghartz et al., "Inert matrices for the transmutation of actinides: fabrication, thermal properties and radiation stability of ceramic

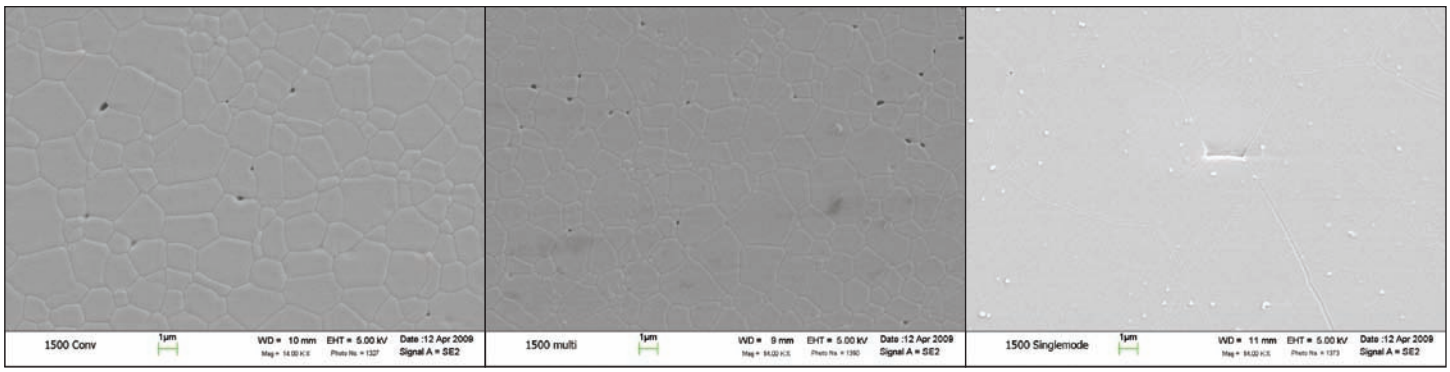

Figure 4. Micrographs showing the grains for conventionally sintered (left), MMM (center), and SMM sintered (right) samples of 8YZ; T = 1500°C.

materials," Journal of Alloys Compounds, 1998, 271,.544.
[8] ASTM C 1327-03. Standard Test Method for Vickers Indentation Hardness of Advanced Ceramics.
[9] ASTM E 112-96. Standard Test Methods for Determining Average Grain Size.
[10] I. Ahmad et al., "Effect of microwave heating on the mass transport in ceramics," Ceramic Transactions, 1993, 36, 287.

About the Author

Andrew is a senior in the Department of Materials Science and Engineering at Virginia Tech. He is on track to receive an official certification in nuclear engineering from the Department of Mechanical Engineering with his Bachelor of Science degree. He was a research assistant in the Microwave Processing Research Facility, under Dr. David Clark and Diane Folz, during the Spring and Summer of 2009. He is primarily interested in the properties, processing and structure of ceramic materials, and is planning to pursue a Master of Science degree in MSE which will focus on research in ceramic materials.

Mechanical Properties Testing of Running Shoes

Stephen Boedicker, Seth Hunter, Patrick Klesmith, Thor Nearn, Paul Spreen
Rose-Hulman Institute of Technology, Department of Mechanical Engineering, Terre Haute, Indiana 47803

Abstract

Mechanical properties testing of running shoes was performed. Stress relaxation tests and energy absorbing tests were performed on excised samples and on unmodified shoes. The stress relaxation moduli for running shoe midsole materials ranged from 19 psi to 114 psi.

Keywords: Running Shoes, Stress Relaxation

1. Introduction

Running shoes are an important part of the athletic-shoe industry, that has annual sales in excess of $7B[1]. Running shoes continue to develop, to address runners' requirements and concerns. Some of the criteria that runners use when purchasing shoes are based on osteomechanical effectiveness, comfort, expected shoe lifetime and cost. Materials used in the shoes, particularly in the soles, affect the shoe properties and it was upon these considerations that this study was based.

Running midsole materials may include polyvinyl acetate (PVA), polyurethane (PU), ethylene vinyl acetate (EVA), isoprene, neoprene or combinations of these polymers. The materials are examples of elastomers (isoprene and neoprene) or thermoplastic elastomers (PVA, PU and EVA). One of the primary functions of the midsole is to absorb energy during running. Running shoe designs incorporate varying combinations of these materials, resulting in shoes with different energy absorbing qualities. Specific polymer formulations are not published, as these are proprietary data. A given formulation is based on mechanical requirements of the shoe design and the available injectable materials at a given shoe manufacturing plant.

Many mid- to high-end running shoes today have midsoles comprised of EVA, PU or a combination of the two. Through different molds and forms, shoe manufacturers use EVA, PU and other polymers in different combinations to achieve the desired properties required by different shoe styles.

2. Procedure

2.1 Stress Relaxation Tests

Stress relaxation tests were performed on samples excised from the heel and forefoot of the shoe midsole. Stress relaxation testing is based on applying an initial load to a sample (tensile or compressive), and holding that strain at a fixed level while monitoring the decrease in load. Stress is calculated by dividing the force (which is relaxing with time) by initial sample area. The output of the tests is force (or stress) as a function of time. A stress relaxation modulus can be calculated if the stress (at a given point in time) for several tests (at different strains) is plotted as a function of strain. The slope of the stress (at time t_o) as a function of strain gives the relaxation modulus (for data taken at t_o).

Figure 1 shows an example of stress as a function of time for a typical compressive trial. The data shown is for a 12.7 mm (0.5 inch) diameter specimens from a running shoe midsole. The intial (fixed) strain applied for the test shown in Figure 1 is 40%.

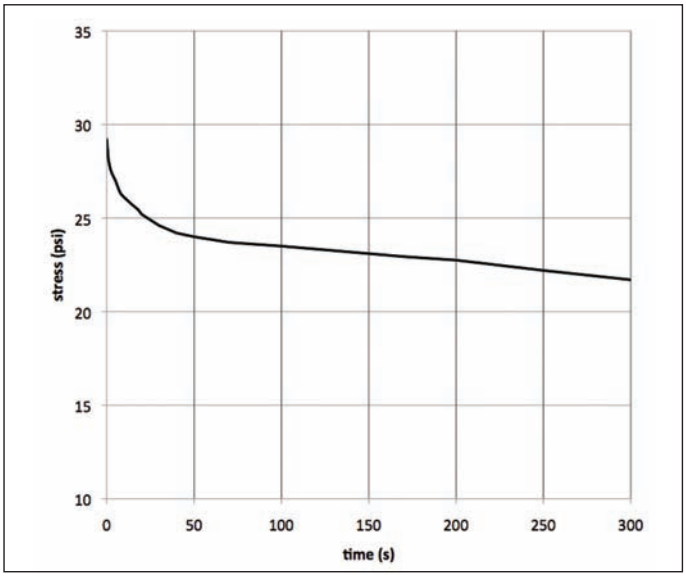

Figure 1. Stress as a function of time for a typical load relaxation test. The data shown is for a 12.7 mm diameter specimen from a Saucony shoe with an initial compressive strain of 40%.

The data shown in Figure 1 is from a Saucony shoe excised sample with a diameter of 12.7 mm. By comparison, other sample sizes that were tested included 7.6 cm diameter samples from from shoe midsoles. Samples were hand ground with coarse sandpaper to have flat, parallel sides. The thicknesses of the samples ranged from 5 to 35mm. The relatively large range of sample thicknesses was a result of whether samples were from the forefoot or the heel of the midsole. Figures 2a and 2b show samples from a heel (Figure 2a) and and a side by side comparison of forefoot and heel samples (Figure 2b).

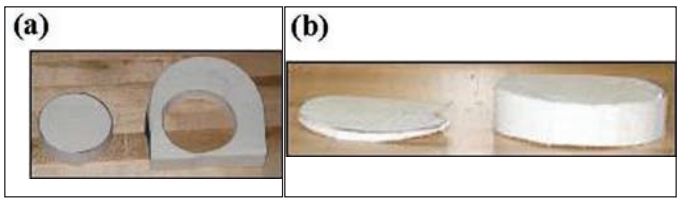

Figure 2 (a) Photo of stress relaxation sample from a midsole heel. **(b)** Photo of stress relaxation samples from forefoot and heel samples. The heel sample is the thicker sample shown on the right. After removing the samples from the midsole, the flat sides were sanded until parallel.

Stress relaxation tests were carried out on a MTS 858 tensile tester using a 2.5N load cell. The samples were placed between two flat metal surfaces (platens), and the samples were given an initial known strain. Initial strains ranged between 10 and 60%. Caliper measurements were taken to measure the distance between the platens before and after the load was applied, to determine the compressive strain on the sample.

In the stress relaxation tests that were performed, two approaches were used to define the time at which stress would be calculated. Some of the data were taken when the load was sixty percent of the initial load. Another group of data were taken after a fixed time of thirty five seconds into the test, regardless of the percent that the load had relaxed.

The types of shoes that were tested included competitive running shoes made by Adidas, Brooks, Saucony, New Balance and Athletic Works as well as other non-running shoe samples. Table 1 shows examples of the types of shoes that were tested.

Table 1. Examples of Shoes that were Stress Relaxation Tested.

Type of Shoe	Cost $	Midsole Material
Saucony Progrid OMNI 7	100	EVA Polymer
New Balance 550	60	EVA Polymer
Athletic Works Journey MW	20	EVA Polymer

2.2 Energy Return Percent Tests

In addition to stress relaxation testing on excised samples, an additional test on intact shoes was performed. Cyclic tests were performed in a tensile tester to calculate a parameter called 'Energy Return Percent' or 'ERP'. The work was based on a previously published standard[2]. One objective of the work was to determine if New Balance's 'Zip' material was significantly different than EVA from other manufacturers, including Asics and Brooks. To conduct the test, a ram of a machined dimension (known as a 'tup') was pressed into the sole of the shoe at the inside heel. Force, time and displacement were monitored to determine the energy into the shoe and the energy returned for each heel strike. Figure 3 shows a schematic diagram of force as a function of displacement for a loading and unloading cycle. The area between the two curves is the energy absorbed by the shoe.

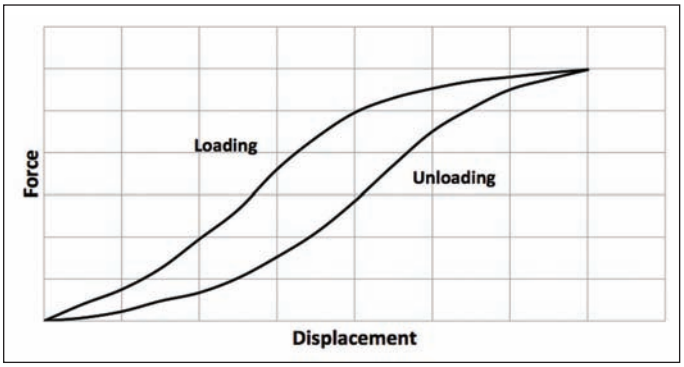

Figure 3. Example of load as function of diplacement during the Energy Return Percent (ERP) tests. The area between the 'loading' and 'unloading' curves represents the energy absorbed. The energy returned is the complement of the ratio of energy out to energy[2].

An ASTM standard[3] requires that the specimen response must be a half sine curve. To achieve a half sine curve response, a pause in the drive is necessary in between cycles due to the viscoelastic effect of the material. The shoe material's inherent viscoelasticity causes the insole to take time in getting back to the 'starting position'. In experimental practice, a two second pause in between full cycles was used.

A constraint on testing was that the initial force into the shoe on each cycle had to be nominally 5 ± 0.5 J. This reference energy is a constraint of the ASTM standard and is measured by taking the product of maximum force and maximum displacement for the hysteresis curve[3].

The shoes that were tested had midsoles made of EVA, neoprene, and Zip. The Zip material was chosen since it was a relatively new shoe material on the market, and extensive claims had been made about its performance[4].

The variability in shoe design is addressed in ASTM F1614-99 standard. According to that standard, a flat span of 45 millimeter diameter is required in the inside heel region of the sole, to allow for the contact surface to be

parallel with the bottom platen upon which the shoe sits during testing. The standard also requires that the thickness of the sole must fall within the range of 5 to 35 millimeters in thickness from the top of the insole to the bottom of the outsole[3].

The performance metric for testing energy into and out of the shoe is a hysteresis energy curve. The values for energy are obtained from the displacement and force through a numerical integration where the energy into the specimen is represented by the top curve of the plot and the energy out of the specimen is the lower curve. The energy lost is the area between the curves, which is the value of interest for the specimen. Energy Return Percent (ERP) is calculated by taking the complement of the difference between the energy applied and the energy returned.

An MTS 858 tensile tester was used to test three shoe samples. Shoe samples were conditioned by running 25 cycles of the displacement function before data was recorded. The 26th through 30th cycles served as data in the analysis. The conditioning helped mitigate the possible effects of initial stiffness[2].

3. Results

Table 2 summarizes stress relaxation moduli for samples from running shoes (Adidas and Brooks) and other non-running shoe samples. For each individual stress relaxation test, the stress was determined when the stress was at 60% of the initial stress. The data shows that the running shoes have a lower stress relaxation modulus than non-running shoe samples.

Table 2. Examples of Shoes that were Stress Relaxation Tested.

Type of Shoe	Cost	Midsole Material
Saucony ProGrid OMNI 7	$100	EVA Polymer
New Balance 550	$60	EVA Polymer
Athletic Works Journey MW	$20	EVA Polymer

Table 3 gives the load relaxation moduli for samples for which stress was determined 35 seconds after the initial application of the load. The data shows that the Saucony ProGrid shoes had the lowest relaxation modulus, and that Athletic Works Journey model had the highest relaxation modulus of the shoes tested. The data suggests that relaxation modulus and cost are inversely related. The data in Table 3 are generally higher than that in Table 2, possibly as a result of a different time used after the start of each experiment for obtaining stress measurements

Table 3. Stress Relaxation Moduli (at time τ = 60% of max).

	Adidas	Boot	Brooks	Old	Sandal	Pink Sandal
E_r (psi)	22.4 ± 0.7	67.6 ± 2.0	18.5 ± 1.2	25.9 ± 0.7	32.7 ± 0.8	25.7 ± 0.5

Table 4. Stress Relaxation Moduli (at time to = 35 s after loading).

	Saucony Progrid OMNI 7	New Balance 550	Athletic Works Journey MW
E_r (35s) (psi)	66 ± 13	83 ± 22	114 ± 28
Cost $	100	60	20

Figures 4 and 5 are example plots of stress (at 35 s) as a function of applied strain. The slopes of the best fit lines shown in each Figure give the relaxation moduli provided in Table 3. Figure 5 is a plot of relaxation moduli as a function of shoe cost, showing an inverse correlation. The purpose of plotting relaxation modulus as a function of cost was to determine if performance (as approximated by shoe cost) cost was a function of stress relaxation modulus. Since cost and relaxation modulus are inversely related, Figure 6 preliminarily suggests that low relaxation modulus correlates with higher performance running shoe midsole materials.

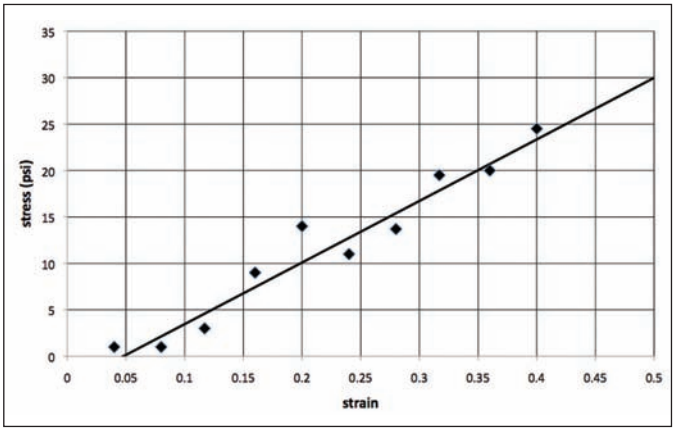

Figure 4. Stress (at 35 seconds) as a function of strain for Saucony shoes. The modulus is 66 psi for the data shown.

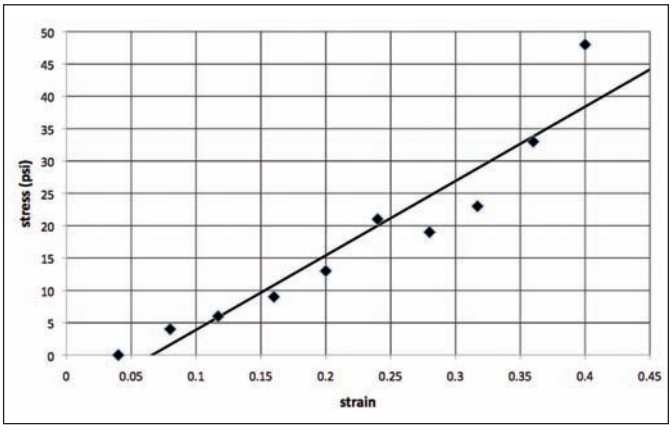

Figure 5. Stress (at 35 seconds) as a function of strain for Athletics Works Journey shoes. A stress relaxation modulus of 114 psi was calculated for this shoe.

Figure 7 shows programmed displacement as a function of time. The relatively small displacement, in the relatively short period of time (~20 ms) ensures that the 5 J energy input requirement is met. An advantage of controlling displacement is that displacement can be programmed as a sine function, a ramp, or any combination. The impact (sine function input) is completed in 30 ms. The actual displacement is different because the tensile tester does not perfectly follow the input function. Displacement can be adjusted to alter both maximum force and total energy applied over a given time period.

Figure 8 shows when the measured force is plotted as a function of displacement for a single impact. The data shown is representative of all of the impacts that were measured. The ASTM standard requires that the impact loading time has to be 15 ± 5 ms[3]. The time between the 10% of the maximum force and the maximum defines the loading time.

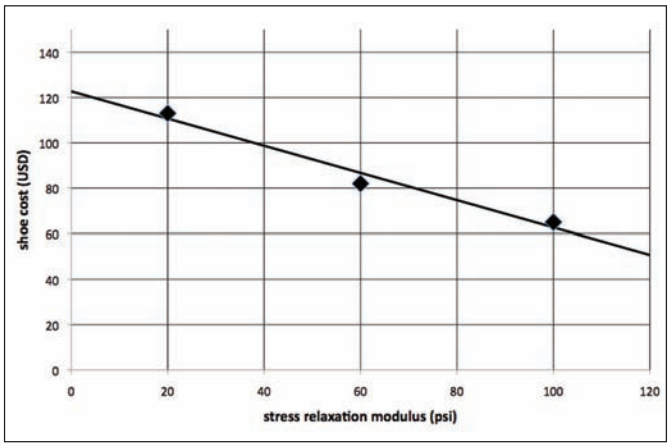

Figure 6. Relaxation modulus (for stresses calculated at 35 seconds after loading) as a function of shoe cost. A linear relationship between modulus and shoe cost is suggested.

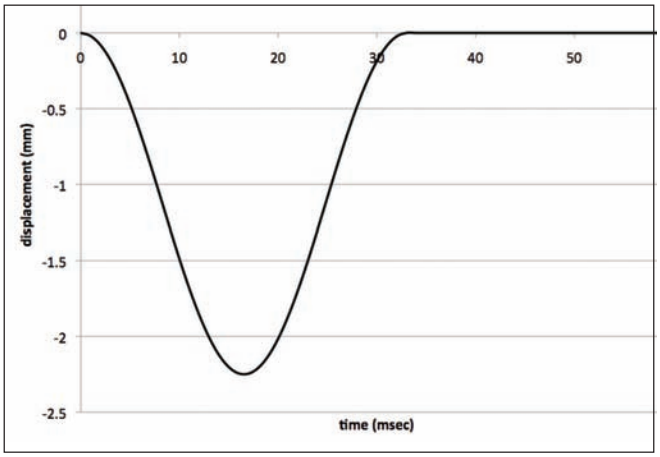

Figure 7. Example of test data, showing programmed displacement as a function of time.

Table 5 gives Energy Return Percent values for the three shoes that were tested. The reference energy input is shown to be within the specification of 5 ± 0.5 J.

Table 5. Energy Return Percent Values for the Three Shoes.

	ERP	Max Reference Energy Input (J)
EVA (Asics)	71.9 ± 1.8 2.5% of value, 95% C.I.	5.07
Neoprene (Puma)	80.6 ± 1.8 2.3% of value, 95% C.I.	4.76
New Balance Zip	72.1 ± 1.8 2.5% of value, 95% C.I.	5.17

4. Discussion

One of the general conclusions that can be made from examining the data in Table 2 is that lower relaxation moduli, for running shoe midsole materials, is correlated with better quality running shoes. For example, the relatively moduli values for Adidas and Brooks shoes are lower than that of work boots and sandals. Another example is seen by correlating the moduli with cost. If cost is an indicator of running shoe quality, then the data shown in Table 3 indicate that a low midsole relaxation modulus is correlated.

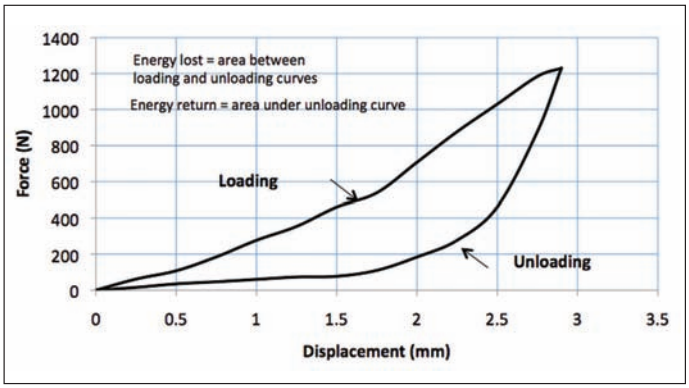

Figure 8. Representative plot of loading and unloading force as a function of displacement. The ERP parameter is the complement of the ratio of energy returned to energy applied.

The Energy Return Percent work showed that neoprene material in the Puma shoe has a higher energy return percentage than the New Balance Zip material, as well as that from the EVA material found in the Asics shoe. Possible future tests can determine if this is a result of the material itself or another factor inherent to the shoe design. Other running shoes can be tested, and more data may suggest whether the preliminary results reported are due to material or shoe design. Another future study may focus on the possible effects of higher energy return percentage. It may not be known whether a higher energy return percentage is always associated with higher performance for running shoes. Rather, an optimum energy return percentage may be possible and could be determined by further testing.

5. Conclusion

Compressive stress relaxation modulus was determined for running shoe midsole materials. Lower modulus appears to correlate with higher performance running shoes. Energy Return Percentage experiments were performed on three types of running shoes. Three brands were tested, and preliminary results indicate that a specific Puma shoe had a higher energy return percentage than the other two shoes tested (New Balance and Asics).

Acknowledgments

The authors are grateful for the faculty and staff at Rose-Hulman. Individuals that provided support during the experimental work and analysis included Prof. Patrick Ferro, Prof. Richard Layton, Prof. David Stienstra, Ray Bland, Gary Burgess, Mike Fulk and Ron Hoffman.

References

[1] Weblink:http://npd.com/corpServlet?nextpage=fact-sheet_s.html, accessed on 11th Nov. 2009.

[2] D. R. Ireland, "The shocking truth about athletic footwear," Standardization News, 1992, 20, 42-45.

[3] ASTM F1614-99, Standard Test Method for Shock Attenuation Properties of Materials Systems for Athletic Footwear, and ASTM F1976-06, Standard Test Method for Impact Attenuation Properties of Athletic Shoes Using an Impact Test

About the Authors

Stephen Boedicker is from Columbus, Ohio and graduated from Olentangy Liberty High School in 2005. He is currently a senior at Rose-Hulman Institute of Technology majoring in Mechanical Engineering. While at Rose-Hulman Institute of Technology, he participated in the varsity track and cross country programs. He worked at the Air Force Research Labs as well as GE during the summer for internships. He accepted a position with GE Consumer & Industrial starting July 2009.

Seth Hunter is a senior mechanical engineering student at Rose-Hulman Institute of Technology in Terre Haute, Indiana. Born and raised in Columbia City, Indiana, Seth plays a very active role on Rose-Hulman's campus, including holding several leadership positions within the social fraternity Phi Gamma Delta, intramurals, and math department grading assistant, all while maintaining a grade point average worthy of the Dean's List for all four years. Outside of the educational realm, Seth has three years of mechanical engineering intern experience at such recognizable companies as Reelcraft Industries and Ingersoll Rand Security Technologies, while also participating in such philanthropic events as Heart to Honduras, Bikes for Tykes, Habitat for Humanity, and TREES.

Patrick Klesmith is a senior mechanical engineering student at Rose-Hulman Institute of Technology in Terre Haute, Indiana. Patrick is graduating with a BS in Mechanical Engineering in May 2009.

Thor Nearn is a senior mechanical engineering student at Rose-Hulman Institute of Technology in Terre Haute, Indiana. Thor is graduating with a BS in Mechanical Engineering in May 2009.

Paul Spreen is a senior mechanical engineering student at Rose-Hulman Institute of Technology in Terre Haute, Indiana. Paul is graduated with a Bachelor of Science in Mechanical Engineering in May 2009.

Physical and Chemical Structural Analysis of Pistachio Shells

Jessica Piness

Virginia Polytechnic Institute and State University, Department of Materials Science & Engineering, Blacksburg, Virginia 24061

Abstract

Pistachio shells were examined to determine structure and chemical composition. Structural analysis was completed using a differential scanning calorimeter (DSC), polarized light microscopy (PLM) and environmental scanning microscopy (ESEM). Chemical composition was quantified with Fourier transmission infrared spectroscopy (FT-IR) for organic components and electron dispersive spectroscopy (EDS) analysis for inorganic matter. The shells were found to have a layered, porous structure. Triglyceride fat and cellulose sugar accounted for most of the natural polymers present. The amount of fats increased inversely to the proportion of sugar closer to the outside surface of the shell, possibly accounting for the transport of nutrients into the shell as opposed to the strength needed from cellulose on the inside edge. Understanding the structure and its elemental derivatives will help in the future quantification of physical and mechanical properties.

Keywords: Pistachio, Cellulose, Biopolymers, Structure

1. Introduction

Nature is filled with polymers. Many are formed by cellulose, which is a compound formed from polymerized chains of glucose. Cellulose has a high degree of hydrogen bonding, creating a very strong, durable polymer[1] (Figure 1). As manufacturing costs for polymers increase due to the scarcity of petroleum, it is hoped that natural alternatives such as cellulose based materials can provide cheaper and more biodegradable products.

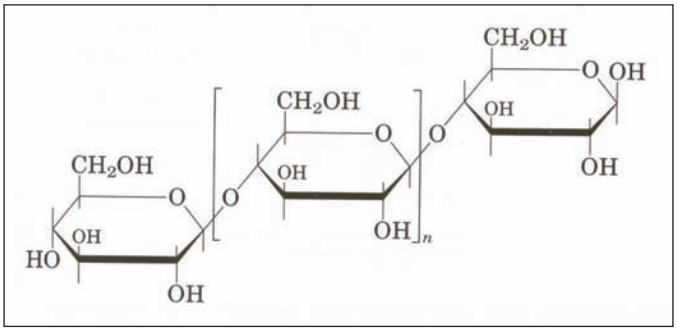

Figure 1. Cellulose, the group in brackets, is an individual glucose molecule2.

Pistachio shells are one example of a very tough natural polymer (Figure 2). The shells are extremely tough for a plant shell, which makes characterization intriguing. As opposed to the actual nuts, nothing was found in the literature about pistachio shells. Therefore, the shell was examined for both structural and chemical information. Analysis was completed on several different areas of the shell to determine if physical and chemical compositions varied with the depth of the shell. Quantifying structure and elemental make-up has the potential to explain many of the unique attributes of pistachio shells, such as their hardness and strength.

Figure 2. (L-R) Inside and outside of a pistachio shell.

2. Procedure

2.1 Shell Preparation

Shells were submerged in water for two weeks to remove salt and any other artificial treatments. Four of the shells were mounted in epoxy and polished up to 0.03 µm for microscopic examination. Two samples were of the cross-section of the shell, and two others were of the inside and outside shell surfaces. All the mounts except one cross-section were sputtered with gold for scanning electron microscope (SEM) and electron dispersive spectroscopy (EDS) analysis. The other cross-sectional sample was preserved and polished for polarized light microscopy (PLM).

2.2 DSC Analysis

Approximately 16 mg of ground shell sample was loaded in a platinum crucible under helium carrier gas in a differential scanning calorimeter (DSC). The sample was heated up to 400 °C and then cooled back to 30 °C at 10 K/min. DSC data was analyzed for structural information and mass loss.

2.3 Microscopy

Both EPI-polarized light microscopy and ESEM analysis were completed to determine the structure of the shells. Polarized light microscopy using EPI, or reflected, light was used for structural analysis of a cross-sectional sample. The other three samples, cross-sectional, inner shell and outer shell surfaces, were sputtered with a thin layer of gold for ESEM analysis. The inner and outer shell samples also underwent EDS analysis to uncover any inorganic chemical differences between the outside and inside of the shell.

2.4 FT-IR Analysis

Solid state FT-IR was performed on small shell fragments around 2-4 mm in diameter. Again, the inner and outer shell surfaces were examined for differences, yet this time in organic chemical composition.

3. Results and Discussion

3.1 Physical Structure

DSC analysis was the first test performed on the shells. This was done in the hopes of determining the glass transition temperature or Tg of the pistachio polymer. A Tg marks the temperature where a polymer transitions from crystalline to amorphous with the addition of thermal energy[3]. A Tg is not normally a fixed temperature, rather it is dependent upon processing[3].

With the pistachio shell fragments, it was difficult to come up a well defined Tg. As seen in Figure 3, the blue line measuring thermal changes of state had several peaks, some better defined than others. This data provides evidence of a very complex structure. Following along to the right, the first couple upper, endothermic, peaks might be lower weight amorphous polymers that eventually transition into higher molecular weight, crystalline sections. To identify the peaks with more certainty, shell fragments would need to undergo x-ray diffraction at temperatures corresponding to the points of interest.

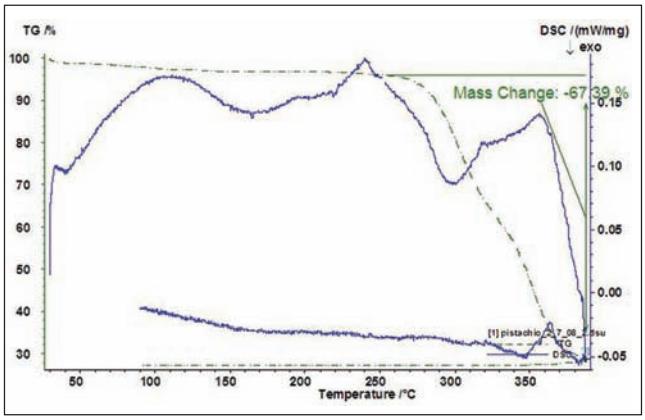

Figure 3. DSC graph for shell decomposition.

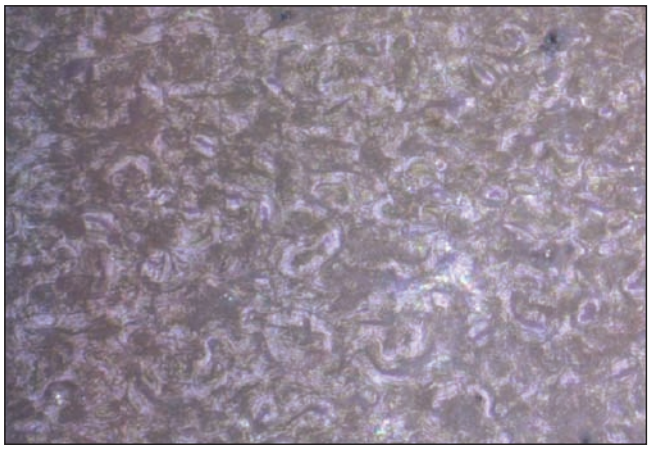

Figure 4. EPI-Polarized Light Microscopy at 20x.

Polarized light microscopy was the optical method used to examine a cross-section shell. Micrographs revealed a fibrous, porous structure. The shinier area towards the lower right corner of Figure 4 is thought to be a region of crystallinity. Analysis by ESEM provided a more in depth picture.

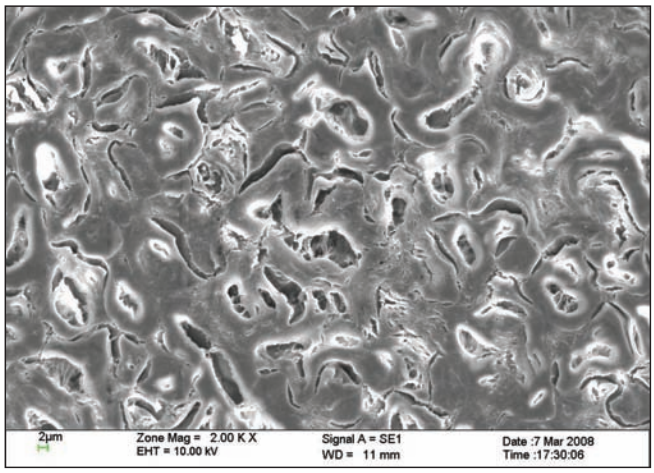

Figure 5. Overall structure from a cross-sectional sample – ESEM at 2000x.

Three samples were examined by ESEM, a cross-sectional slice of shell, the outside shell surface and the inside shell surface. Figure 5 provides a good example of a representative cross-sectional structure. The pores are probably due to the need to transport nutrients and oxygen to and from the growing pistachio nut.

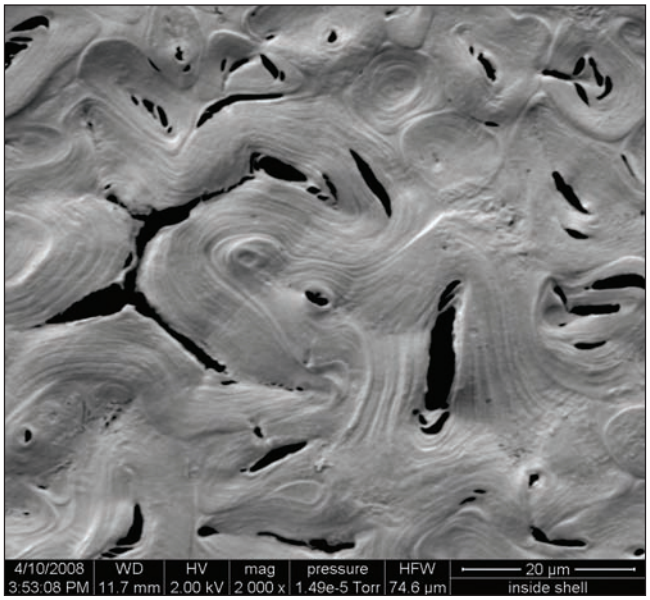

Figure 6. Inside shell structure – ESEM at 2000X.

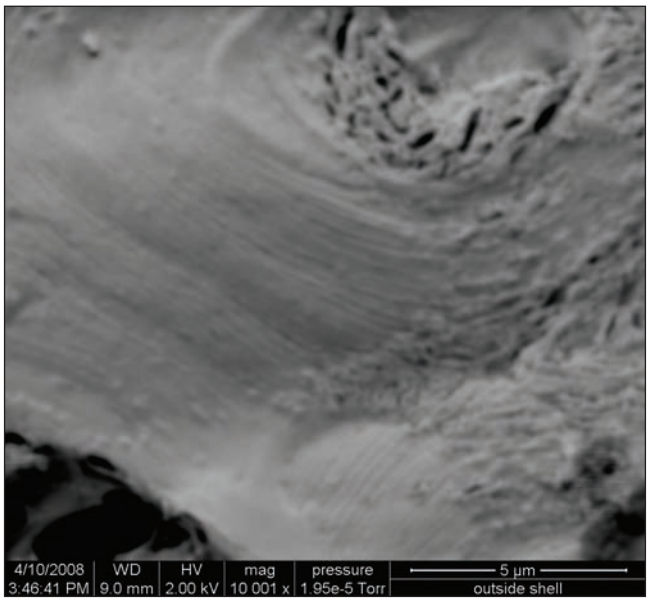

Figure 7. Outside shell with laminar features – ESEM at 10000X.

Figure 6 shows a large pore with its surrounding inside shell surface. As seen in Figure 6 and in more detail in Figure 7, layering was very evident producing a laminar structure flowing around the pores. This reflects common polymeric growth of sections of different polymers bordering on each other[4]. However, the sample was very sensitive to the ion beam from the ESEM at high voltage. This caused problems as the samples visibly deformed under high magnification. Therefore, it was impractical to try EDS analysis or any other sort of close examination to find out whether the structure in Figure 7 is a compilation of layers of different polymers or the same polymer folded on top of itself.

3.2 Chemical Analysis

Also, the chemical composition of the shell was examined. IR analysis revealed a make-up of fats and polysaccharide cellulose carbohydrates. Cellulose provides strength and organization to the shell, whereas fats help to dissolve nutrients and vitamins necessary for plant growth[1]. Fat peaks[5] generally show up by detection of C-H bonds around 3000-2800 cm^{-1} and C=O bonding between 1745-1725 cm^{-1}. Carbohydrates such as polysaccharide cellulose have defining peaks in spectra at 3000-2800 cm^{-1} for C-H bonds and 1400-800 cm^{-1} from bonds between glucose polymer chains[5]. The spectra of the inside shell showed the definite presence of cellulose and carbohydrates with sharper, better defined peaks in the 3000-2800 cm^{-1} range and a multitude of peaks starting at 1700 cm^{-1}. This may note the linkages between glucose polymer chains to create cellulose. Some protein was also detected with amine peaks between 1700 and 1600 cm^{-1}. The lower spectra in Figure 8 is the result for the outside shell. The spectra of the outside shell surface appears to have a higher concentration of fat with sharp peaks at 2920 cm-1 and 1720 cm^{-1} as seen in the top graph in Figure 8.

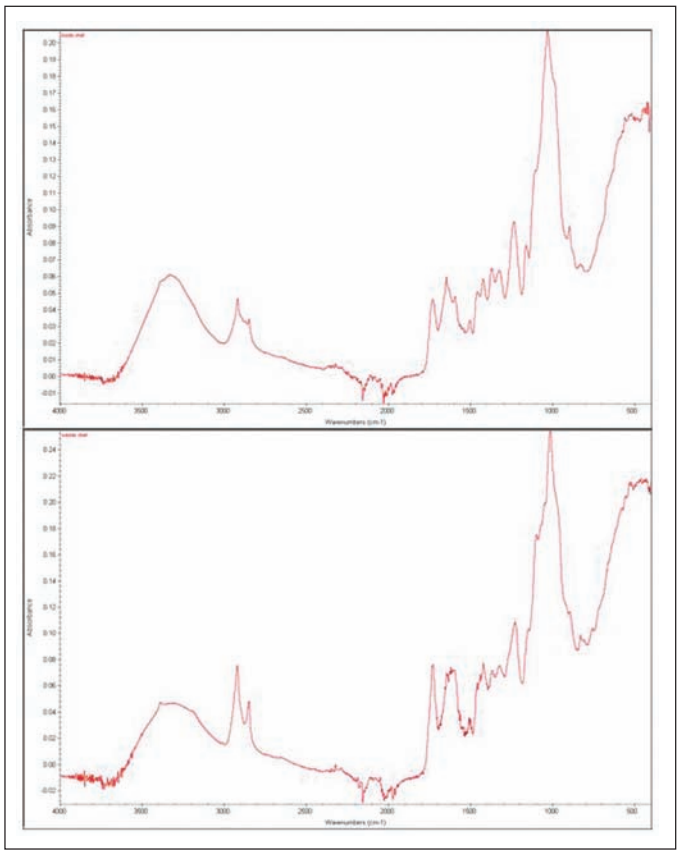

Figure 8. IR analysis for inside shell surface (top) and outside shell surface (bottom).

The change in composition between shell surfaces probably accounts for the need for a strong, protective structure

provided on the inside of the shell by cellulose. In contrast, fat on the outside of the shell helps dissolve vitamins and nutrients for transport to the nut. Traces of protein and further fats found on the inside surface may be related to the protective membrane formed around the nut.

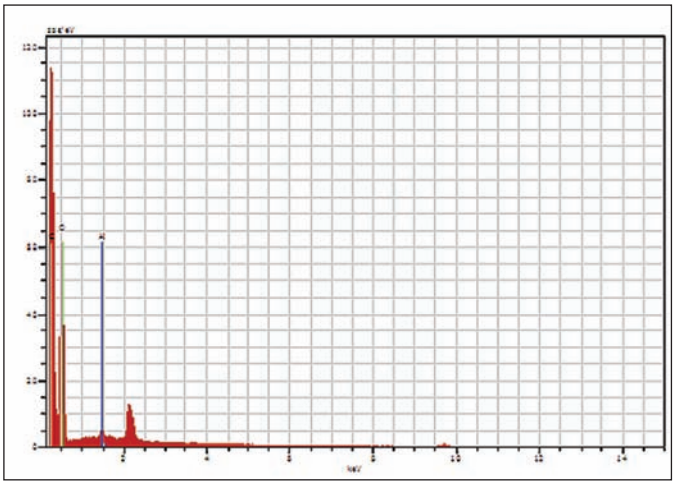

Figure 9. Example EDS analysis of inside shell surface.

EDS results from the ESEM showed no measureable traces of inorganic matter in the shell, no matter the surface. As shown in Figure 9, the only elements detected were carbon and oxygen. The aluminum present is probably due to the near impossibility of removing all alumina from the polishing process from such a porous sample.

4. Conclusions

In conclusion, pistachio shells have a very fibrous structure with a combination of amorphous and crystalline polymers. From microscopy, the shells were found to have laminar polymer layers wound around pores. Chemically, pistachio shells appear to be made from triglycerides and cellulose with no trace inorganic compounds. The concentrations of triglyceride and cellulose vary as per the depth of the shell in accordance with the function of the shell at that depth. These results, especially those quantifying the physical structure, provide a good foundation for explaining the results of future mechanical testing.

Acknowledgements

This research was performed at Virginia Tech with the suggestion of Dr. Alex Aning in the Department of Materials Science and Engineering. Thanks are due to Dr. Aning for the willingness to allow me to participate in research and to his graduate students, Andrew Zeagler and Niven Monsegue for help with laboratory procedure. Mr. David Berry was invaluable for equipment training. Dr. Steve McCartney at ICTAS assisted with ESEM imaging, and Dr. Justin Barone of Biological Systems Engineering helped with FT-IR use and results analysis. Special thanks also to Ms. Denise Russell, Mr. Chris Wilcox and Mr. Thomas Piness for polarized light microscopy, SEM images and DSC results analysis done at Bosch Charleston.

Reference

[1] R. M. Brown Jr., et al., "Molecular and Structural Biology;" Springer: Dordrecht, 2007.

[2] Weblink:http://erkki.kennesaw.edu/schem219/sc00029.htm Lesson four: polysaccharides and carbohydrate digestion., part of online resources for chemistry courses at Kennesaw State University, accessed on 29th Apr. 2008.

[3] W. D. Callister Jr.; "Materials Science and Engineering: An Introduction," Wiley, New York, 2007.

[4] Weblink:http://www.doitpoms.ac.uk/tlplib/polymers/index.php Crystallinity in Polymers, part of materials science focused teaching packages from the University of Cambridge, accessed on 18th Apr. 2008.

[5] B. Stuart, "Infrared Spectroscopy: Fundamentals and Applications;" Wiley, Sussex, 2004.

About the Author

Jessica Piness is a junior in Materials Science and Engineering and Chemistry at Virginia Tech with a focus in polymers. She enjoys research and working in the laboratory.

Developing Functional Inks for Direct-Write Systems

Mitchell Rodriguez

South Dakota School of Mines and Technology, Department of Materials and Metallurgical Engineering, Department of Mechanical Engineering, Rapid City, South Dakota 57701

Abstract

The field of Flexible Printed Electronics (FPE) carries great potential in reducing manufacturing costs and increasing versatility. The purpose of this research is to explore various ink chemistries and their suitability for deposition with regards to FPE. Titanium ceramics and silver-titanium-iron nanoparticles were utilized for their potential photocatalytic properties. The resulting inks experienced phase separation or hydrolyzed upon exposure to moisture, suggesting that a surfactant-based synthesis would better improve the inks' durability.

Keywords: Thin Film, Titanium Dioxide, Nanotube, Photocatalysis

1. Introduction

Researchers in various fields are actively pursuing direct-write deposition technologies as critical components in various applications, ranging from consumer electronics to medical implants. Direct-write deposition is a form of physical deposition that includes inkjet and aerosol spray methods, in which functionalized "inks" are deposited on a substrate. This procedure can be accomplished in ambient conditions, allowing for the use of flexible substrates as the basis for FPE. Among the various advantages of direct-write technologies, the reduced cost and potential for FPE are among the most significant. However, the lack of a variety of well-established ink formulations has led to an effort by academia and industry alike to develop the necessary functional inks.

Organometallic Ti-based inks were pursued for a number of reasons. First, the ability to decompose the metal oxide via certain conditions (in this case, exposure to moisture) gave the user additional control over the properties of the material; it allowed the user to take advantage of the organometallic material's easy dispensability while providing the option to convert to the functional TiO_2 material that is often used in photocatalytic, semiconductor and biomedical applications[1]. Second, the Ti-based organometallic material had steric resemblances to other organometallics with metals other than titanium – theoretically it could be feasible to use the same or similar approach to deposit other metal oxides in such a fashion. For example, Willis et al have developed methods of using metal acetylacetonates as the basis for metal oxides via solvothermal synthesis[2]. Sol-gel approaches were the preferred method as they could be performed at ambient temperatures and without the need for complicated or expensive equipment[3].

The Fe-doped silver-titanium nanoparticles provided another possible functional ink. In this case, they had potential in photocatalytic operations, specifically visible-light photocatalysis. Their advantages lay in their stability and increased shelf-life[4].

Titanium dioxide nanotubes were pursued for their effectiveness in photocatalytic processes[3,5]. A surfactant-based approach was attempted in order to make a more stable suspension of TiO_2 nanotubes for ink deposition. The surfactant approach was based on the possibility of exploiting surface chemistry to induce controlled, reversible, structural changes to the TiO_2 nanotubes, greatly affecting their photocatalytic functionality[6].

2. Experimental Procedure

The Optomec Maskless Mesoscale Materials Deposition® (M3D) (Optomec, Inc., Albuquerque, NM) system and the Sono-tek Ultrasonic Spray deposition systems (Sono-tek Corporation, Milton, NY) were used for the tests. These instruments were housed in the PEARL (Printed Electronics Applied Research Laboratory), located at the South Dakota School of Mines and Technology. In addition, PEARL's Zeiss Microscope viewer and Scanning Electron Microscope (SEM) were used to characterize the materials.

The solutions were deposited in ambient conditions onto a Kapton® (DuPont, Wilmington, DE) polyimide surface. No laser curing or subsequent heat-treatment was conducted on the samples. The samples were atomized prior to deposition. A detailed explanation of the various syntheses follows.

2.1 Titanium Precursor Inks

Using a sol-gel process as the inspiration for the TiO_2 precursor ink[7], the following synthesis was attempted (this will be subsequently called TiO_2 precursor ink 1): Add 0.62 g PVP (polyvinylpyrrolidone, MW ~55,000 Da, Sigma-Aldrich) to 16 mL EtOH (Ethanol, Denatured, Reagent Grade, Sigma-Aldrich). Next, add 12.5 g titanium (IV) oxyacetylacetonate (Sigma-Aldrich), followed by an additional 24 mL EtOH to homogenize the solution. Mix the entire solution at 300 RPM for 12 hours at room temperature. A second form of the precursor ink was attempted, using this synthesis (subsequently called TiO_2 precursor ink 2): Add 5 mL of titanium (IV) isopropoxide (TTIP, Sigma-Aldrich) to 125 mL toluene (Sigma-Aldrich). Add 1.5 g PEG (polyethylene glycol) to assist in material dispersal, and mix the entire solution at 300 RPM, 100 °C, for 1 day. A third form of titanium precursor used the titanium (IV) isopropoxide solution as-is (subsequently called TiO_2 precursor ink 3).

2.2 Iron-doped Silver-titanium Core-shell Nanoparticles

Using a sol-gel process[4], the following was synthesized: Add 3 mL of hydrazine solution (Sigma-Aldrich) to 120 mL of 1 mM cetyltrimethylammonium bromide (CTAB, Sigma-Aldrich) aqueous solution. Stir mixture for 1 minute at room temperature. Add 3 mL of 50 mM aqueous silver nitrate ($AgNO_3$, Sigma-Aldrich). The solution should turn a dark brown, similar to coffee. Next, stir for 10 minutes to ensure completion of the redox reaction. Then, add varying amounts of titanium (IV) isopropoxide to the mixture; in this case, 20 mL of a 1 mM TTIP solution in ethanol (reagent grade, Sigma-Aldrich) was added. Stir vigorously for 10 minutes at room temperature. Finally, add 0.00484 g of iron (III) nitrate ($Fe(NO_3)_3$, Sigma-Aldrich) to the mixture to introduce iron into the nanoparticle solution, and stir vigorously for 10 minutes at room temperature.

2.3 TiO_2 Nanotubes in a Surfactant Solution

This also used a reported nanotube synthesis[3], slightly modified to take advantage of surfactant-based solutions. The synthesis was as follows: Add 1 g of TiO_2 nanopowder (99.9%, ~25 nm, Sigma-Aldrich) to a 10 M aqueous sodium hydroxide solution, and heat the solution at 110 °C for at least one day. Filter the TiO_2 nanotubes and mix 1.28 g into an aqueous solution of 10 mL H_2O and 0.3 mL Surfynol® (CT-136) dispersant. Add a few drops of Surfynol® defoamer as necessary in order to mitigate excess foaming. Shake mixture vigorously for at least three minutes to maximize the surfactant's effectiveness.

3. Results and Discussion

Table 1 compares the various inks and their performance in the Optomec M3D® system and the Sonotek system. Notable was the rate of phase separation in some of the systems, most particularly the Fe-Ag-Ti nanoparticles.

The Ti precursor inks experienced rapid hydrolysis rates, in which the TTIP hydrolyzed quickly in the presence of moisture in the air, forming the desired TiO_2 and organic byproducts. However, the TiO_2 thus precipitated, and because of the rapid rate of reaction, the precursor ink would often clog the system as it was exposed to moisture within the deposition tubes; this resulted in no deposition, as shown in Table 1. This was mitigated by using organic solvents.

Table 1. Comparison of Ink Performance on Selected Systems (Kapton Polyimide Substrate).

Functional Ink	**Optomec M3D system (Time until phase separation, consistency of deposition)**	**Sonotek System**
TiO_2 precursor ink 1	5 minutes, inconsistent	N/A
TiO_2 precursor ink 2	11 minutes, inconsistent	N/A
TiO_2 precursor ink 3	35 minutes consistent	N/A (hydrolyzed in system
Iron-doped Ag-TiO_2 nanoparticles	N/A	3 minutes, inconsistent
TiO_2 nanotubes in Surfynol CT-136	<30 seconds, inconsistent	N/A

In the case of the Fe-Ag-Ti nanoparticles, the combined ethanol/aqueous solvent may have been responsible for facilitating a rapid phase separation. This is evidenced by the nanoparticle ink's performance on the M3D® system, where the phase separation was so rapid that it clogged the system almost immediately, resulting in no deposition; this differed from the issues that the Ti precursor inks experienced.

The most effective of the precursor materials was the ink 3, which used the TTIP in its original organic solution. Table 1 shows that ink 3 had the longest uninterrupted deposition period (35 minutes), and a qualitative analysis showed a significantly more consistent deposition pattern than the other Ti precursors. Figure 1 shows the deposition test shapes sampled. Since multiple passes were made in Figure 1, a qualitative analysis indicates that consistency and continuity in the deposition path can be maximized with increasing the number of passes, even if the individual passes occasionally suffer from inconsistency. As shown in Figure 2, the material showed considerable cracking in the material surface, possibly caused by stresses induced in lower layers as ambient moisture seeped into the ink deposition. Despite this, qualitative results demonstrated that the material adhered very well to the polyimide surface.

Based on the performance of the Ti precursor inks as indicated in Table 1, controlling the rate of hydrolysis will be of importance. One method to do this would be to control the level of interaction with moisture by depositing the material in a vacuum; however, depositing the precursor in a vacuum may introduce new issues that did not exist with ambient atmospheric deposition. The alternative is to control the rate of hydrolysis directly; to this end, Dunuwila et al have devised promising methods of controlling the rates of hydrolysis in Titanium (IV) Isopropoxide8, which will be investigated in the future as a possible solution.

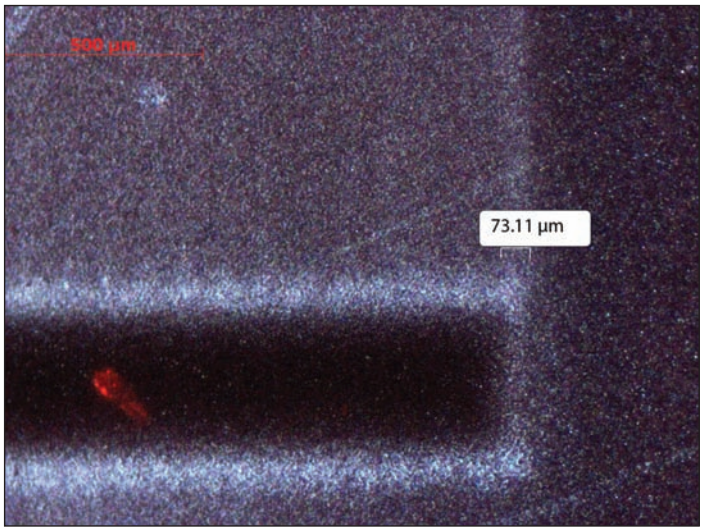

Figure 1. Section of test sample deposition of precursor ink 3 on Kapton® substrate, 133X magnification. Note faint demarcations between depositions.

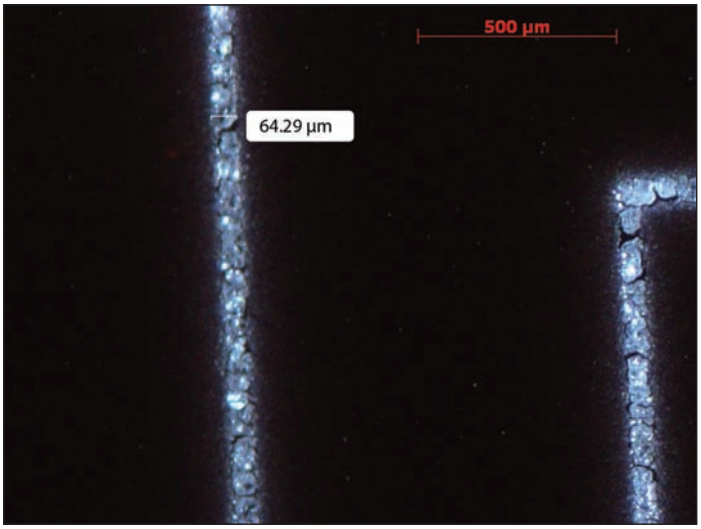

Figure 2. Deposition of precursor ink 3 on Kapton® substrate, 134X magnification. Note significant cracking on surface of deposition.

The iron-doped silver-titanium nanoparticles experienced significant phase separation. This may be attributed to issues with the ethanol having trouble atomizing in the solution. A solution to this problem is to use a surfactant-based approach and changing the solvent to accomplish two goals: improve the suspension of the nanoparticles, and improve the atomization process. SEM images, as in Figures 3 and 4, revealed a breakdown in the spherical structure of the particles, although this may be attributed to the SEM charging the conductive nanoparticles.

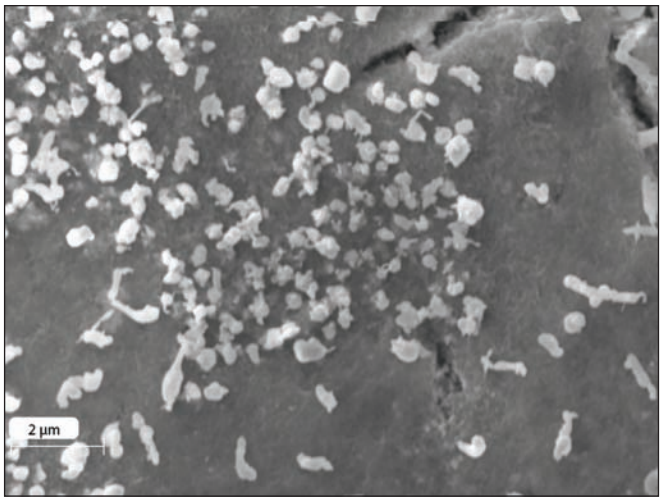

Figure 3. SEM image of silver-titanium-iron nanoparticles at 19,200X magnification.

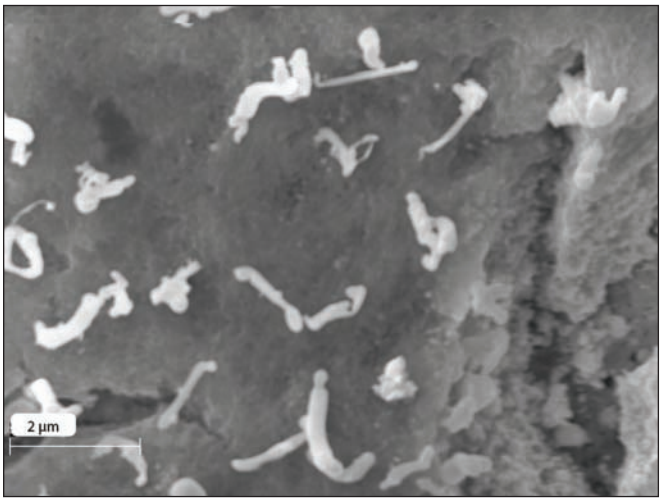

Figure 4. SEM image of silver-titanium-iron nanoparticles at 26,870X magnification.

With the titanium nanotubes, the same issue of rapid phase separation occurred as with the silver nanoparticles, and thus the ink development has experienced considerable setbacks. Most notable was the nanotubes' tendency to rapidly precipitate due to their size. In addition, extended periods of exposure to NaOH caused larger nanotubes to form on the order of microns in diameter as shown in Figures 5 and 6. It is possible that multi-walled nanotubes were being formed in the presence of the NaOH solution, due to the curling induced by the deprotonated environment[6,9]. Several approaches are being considered to resolve this issue, including the use of surfactants optimized for metal oxides (specifically Surfynol CT-324) and using mechanical methods to prevent particle agglomeration (additional ultrasonication, etc.).

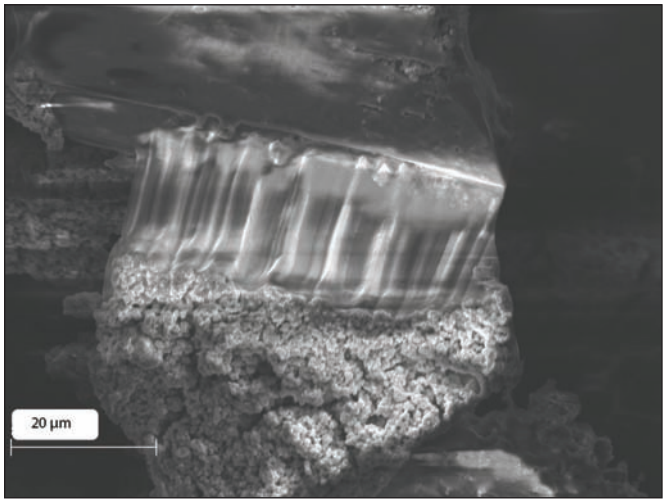

Figure 5. SEM image of TiO_2 nanotubes, 2990X magnification. Note size of TiO_2 nanotube diameters (~2 micrometers).

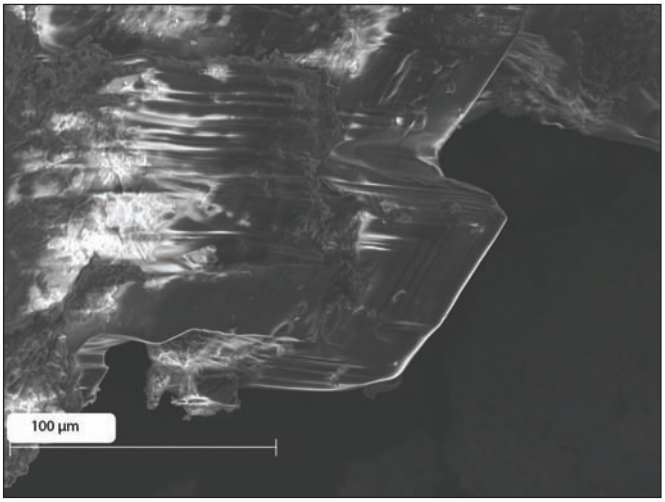

Figure 6. SEM image of array of TiO_2 nanotubes, 1100X magnification.

4. Conclusion

Attempts at deposition of the above materials indicate that problems with phase-separation and rapid hydrolysis must be addressed before the inks can be viable. In addition, surfactant-based approaches will be further investigated to see if they can help significantly improve the viability of the inks. Issues to consider in future work include controlling the rate of hydrolysis and phase separation, to the point where the material will retain its consistency until the actual deposition. Furthermore, methods of curing the depositions to increase their functionality will be investigated.

Acknowledgements

This material is based upon work supported by the National Science Foundation/EPSCoR Grant #EPS-0554609 and by the State of South Dakota. The author would like to thank Dr. Jon Kellar and Dr. Shawn Decker for their support, mentoring and use of facilities. In addition, the author would also like to thank PEARL, Mr. James Randle and Mr. Ryan Wendt for technical support regarding the instruments.

References

[1] K. C. Popat et al., "Titania nanotubes: A novel platform for drug-eluting coatings for medical implants?," Small, 2007, 3, 1878-1881.

[2] Willis et al., "Metal acetylacetonates as general precursors for the synthesis of metal oxide nanomaterials," Journal of Nanomaterials, 2007, 1-7.

[3] L. Q. Weng et al., "Synthesis and characterization of nanotubular titanates and titania," Elsevier, 2006, 26, 1405-1409.

[4] W. Wang et al., "Preparation and photocatalytic properties of Fe3+-doped Ag@TiO2 core-shell nanoparticles." Journal of Colloid Interface Sciences, 2008, 323, 182-186.

[5] G. K. Mor et al. "Use of highly-ordered TiO2 nanotube arrays in dye-sensitized solar cells," Nano Letters, 2006, 6, 215-218.

[6] A.S. Barnard et al., "Prediction of TiO2 nanoparticle phase and shape transitions controlled by surface chemistry." Nano Letters, 2005, 5, 1261-1266.

[7] J. A. Lewis et al., "Sol-gel inks for direct-write assembly of functional oxides," Advances in. Materials, 2005, 1-5.

[8] D. D. Dunuwila et al., "Application of controlled hydrolysis of titanium (IV) isopropoxide to produce sol-gel derived thin films," Chemistry of Materials, 1994, 6 (9), 1556–1562.

[9] A. Barnard et al., "Multi-scale modeling of titanium dioxide: controlling shape with surface chemistry." Reviews in Advanced Materials Science, 2005, 10, 21-27.

About the Author

Mitchell Rodriguez is a senior at the South Dakota School of Mines and Technology. He is pursuing a Bachelor dual-major degree in Mechanical Engineering and Materials & Metallurgical Engineering, and will graduate in the spring of 2010. He conducted research through the EPSCoR project for three summer internships. He enjoys reading, swimming and playing his electric guitar when not immersed in work.

A New Method of Generating and Storing Hydrogen for Fuel Cell Applications

Ian M. Fuller

Nanotek Instruments, Inc. Dayton, Ohio, 45404
Wright State University, College of Engineering and Computer Science, Dayton, Ohio 45435

Abstract

Current hydrogen technology relies on natural gas to generate the hydrogen and high pressure gas tanks to store the hydrogen. The new process illustrated here eliminates the negative aspects associated with these processes. Sodium borohydride, or any other metal hydride, is stored in solid form, thereby creating the most energy dense scenario as well as allowing for the use of current infrastructure. However, instead of using a precious metal catalyst, a cheap solid acid such as citric acid, is added to the metal hydride to regulate hydrogen production. With this method, a solid metal hydride/acid powder can be stored under low pressures until hydrogen is needed. At that point, water created from the fuel cells can be added in controlled amounts to the metal hydride/acid powder creating a controllable, humidified hydrogen flow perfect for fuel cell applications.

Keywords: Sodium Borohydride, Fuel Cell, Hydrogen, Hydrogen Economy

1. Introduction

There has been a considerable effort over the past several years to bring hydrogen fuel cell technology to the masses. Through both public and private initiative, fuel cell research and development has yielded vast improvements over fuel cell stacks of previous years. Although several different types of fuel cells exist, classified by the type of fuel they require and the means by which they utilize this fuel, the proton exchange membrane fuel cell (PEM) has become the standard when talking of small scale power generation (<250kW). The PEM utilizes direct hydrogen and oxygen gas to create power by way of a proton conducting membrane. Such a membrane isolates the protons from the hydrogen, allowing them to flow through the thickness of the membrane. The electrons, also from the hydrogen, are then forced through wires creating electrical power. The protons, electrons, and oxygen from a separate gas, typically air, are then combined to complete the reaction and create pure water. As noted, the only byproducts from this method of generating power are heat and water.

The PEM has been slotted for use in vehicle and portable applications for a variety of reasons. The PEM is typically considered to have the highest energy density of any fuel cell[1]. This fact, along with its fast start up time (<1 sec) and relatively low operating temperature has led many to believe that this is the future of portable power generation[1]. However, a single PEM fuel cell, by itself, does not create the necessary voltage or power for use in any meaningful application. For this reason, it is necessary to stack several individual cells together in order to obtain the necessary voltages and power[2].

1.1 Challenges Remain

While the future for PEM technology appears bright, several key issues must be resolved before widespread adoption of this technology can take place, not the least of which is the production and distribution of the hydrogen fuel. Current thought revolves around natural gas reformation and other methods to generate the hydrogen and then compressed gas cylinders to store it. This is a proven technology, but it is not an ideal candidate for PEM fuel cells. For the greatest efficiency, the hydrogen needs to be humidified before entering the fuel cell. When using compressed hydrogen, this feat is accomplished using external humidifiers which add to the cost, power requirements, and complexity of the system. Furthermore, the use of high pressure (up to 10,000psi) hydrogen stored on vehicles leads to questions about the safety of such a technology. As 95% of the hydrogen currently produced in the US comes from steam-methane reformation (SMR) it will eventually be necessary to find a more ecologically friendly method of production[3]. The lack of a single technology for all applications (transportation, portable, etc.) creates a fragmented technology system where each different application requires a different technology. This leads to a higher priced system and a steeper learning curve for any potential customers.

1.2 The Complex Hydride

An emerging school of thought centers on a form of hydrogen storage known as complex hydrides, wherein hydrogen is stored in the bonds within the chemical and is released during a chemical reaction. One such complex hydride receiving a great deal of attention is sodium borohydride ($NaBH_4$). This chemical is relatively inexpensive and has the capability to be mass produced as a derivative of borax. When added to water sodium borohydride reacts to produce hydrogen gas and an environmentally friendly sodium metaborate ($NaBO_2$) as seen in the following reaction[4]:

$$NaBH_4 + 2H_2O \rightarrow NaBO_2 + 4H_2$$

As illustrated, borohydrides in general benefit by deriving two hydrogen molecules from the borohydride itself and two additional molecules from the water it reacts with. This creates a theoretical hydrogen density of almost 11% when the sodium borohydride and a corresponding amount of water are reacted[4]. However, conventional wisdom had been to store the sodium borohydride within a caustic solution of sodium hydroxide (NaOH) and water. The caustic additive worked to slow the reaction between the water and the borohydride; allowing for a safer and longer lasting product. When hydrogen was needed, a platinum or other precious metal catalyst was brought into contact with the solution and hydrogen was released[5]. This approach successfully utilized the sodium borohydride reaction, but the full potential of the chemical as a hydrogen storage medium was not achieved. Expensive precious metal catalyst, low hydrogen content per volume due to large percentages of caustic additives, as well as limited solubility of the sodium borohydride all create problematic issues when this technique is employed in a consumer friendly way.

2. Procedure

A new procedure that may lead to a workable hydrogen economy employs sodium borohydride in solid form, as opposed to a caustic solution. Normally, when sodium borohydride is added to water, hydrogen is produced. However, this rate of production of hydrogen is insufficient to power a fuel cell of reasonable size. For that reason this technique utilizes a solid acid as a reaction controlling agent. Previous techniques have used a caustic ingredient to retard the reaction. This technology, however, allows an inexpensive solid acid, such as citric acid, or a metal salt, such as nickel chloride, to be used to accelerate the reaction to levels adequate for fuel cell use[6]. Typically, the solid sodium borohydride and reaction controlling agent would be placed together in a low humidity container until needed. This is possible as there is no reaction between the powders until water is added. When hydrogen is needed, water may be added in controlled amounts until the desired quantity of hydrogen is produced. This allows the hydrogen to maintain a solid form as long as possible, requiring no high pressures or high temperatures. Furthermore, the hydrogen is able to stay in the densest form until needed in order to conserve space.

Initial results to determine the amount and rate of hydrogen produced were carried out by collecting the hydrogen over water. The solid fuel is reacted with excess water. The created hydrogen is then led through plastic tubing to a graduated container inverted in a bath of water. The hydrogen gas displaces the water in the container, and from periodic measurements, the rate of hydrogen production can be calculated. Such experiments were performed using different combinations and concentrations of solid acids and borohydride at or close to standard temperature and pressure. The sodium borohydride was procured from MP Biomedicals, LLC while the acids were purchased from Spectrum Chemicals & Laboratory Products. The results were then plotted verse time to show the rate of hydrogen production and compared to hydrogen generation rates without the acid controller.

It was also necessary to determine the humidity and composition of the hydrogen gas. This was necessary in order to determine the viability of using the borohydride/acid fuel for hydrogen fuel cells. The TSI Model 7565 Q-Trak from Argus-HAZCO was used to determine the relative humidity of the produced gas as well as to determine any extraneous carbon gases created from the reaction[7]. The Q-Trak was utilized to measure different quantities in the gas created from different fuel concentrations. While the CO sensor was not able to be utilized due to its cross-sensitivity to hydrogen gas, the CO_2 showed no increase in concentrations over the base line. The lack of CO_2 supported the assumption of a lack of CO emissions.

3. Results and Discussion

This technique of adding a solid acid does more than just increase the reaction rate. Previous attempts to use solid borohydrides have resulted in a situation known as caking.

Caking occurs when a layer of the reaction product, sodium metaborate, forms on top of the unreacted sodium borohydride, effectively cutting off any reaction. By increasing the reaction kinematics, the citric acid effectively eliminates all caking issues by churning and bubbling, thereby mixing the metaborate into the powder. The hydrogen produced by this reaction is ideal for fuel cell applications. The reaction rate can be controlled by using different acids at different concentrations and, as the reaction environment remains acidic for longer, a greater percentage of the theoretical hydrogen can be liberated. This relationship between hydrogen production with and without an acid control agent can be seen in Figure 1. Figure 1 shows the hydrogen liberation rate for the reaction between sodium borohydride and excess water (Blue) and sodium borohydride with 50% citric acid by weight and excess water (Red). With most fuel cell systems, an

external humidifier is necessary to humidify the hydrogen gas before it enters the fuel cell.

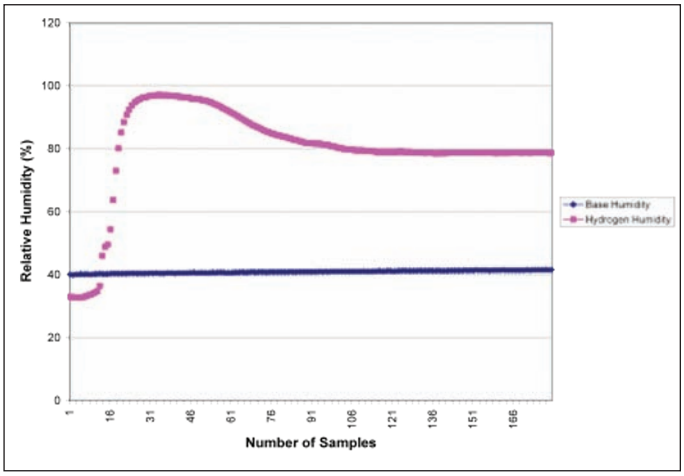

Figure 1. Hydrogen liberation comparison of $NaBH_4$ with and without acid agent and hence reduced nonlinearity.

This humidity helps increase the efficiency and lifetime of the PEM membranes. However, it has been found that the addition of an acid eliminates the need for such equipment. The hydrogen produced from the reaction between the sodium borohydride, acid, and water produces pre-humidified hydrogen void of any gases that may poison the fuel cell such as CO. This pre-humidified hydrogen is also able to achieve relative humidity greater than that of most electrical humidifiers, almost 100% relative humidity. Figure 2 illustrates a comparison of relative humidity between hydrogen produced with 50% acid and gas produced without the agent.

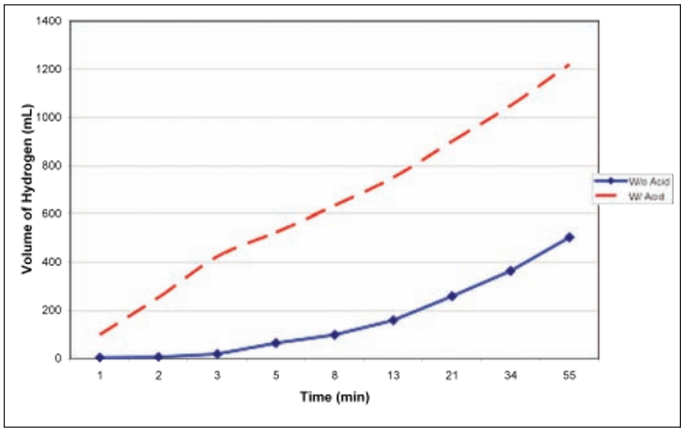

Figure 2. The relative humidity of a hydrogen sample taken at STP. The hydrogen was produced using a 50% acid by weight sodium borohydride/citric acid fuel with excess water.

Both of these figures illustrate the benefits to the hydrogen gas with an addition of 50% acid. It is important to note that the same benefits have been observed in concentrations of as little as 5% acid by weight. This allows for a wide variety of applications to be met with a single technology. The acid concentrations, and therefore, the rate of hydrogen production can be customized to meet the needs of the fuel cell or application.

A low power fuel cell stack may only require a 5% acid concentration. This low acid concentration would allow hydrogen to be created at a slower rate as needed for the stack. The hydrogen is maintained as a solid to provide the greatest energy density. The higher acid percentages would be used for a higher load system. An automobile would require a higher, more dynamic fuel system. Water may be added to this fuel in differing amounts depending on the requirements of the stack.

4. Conclusions

The addition of a solid acid to borohydrides, sodium borohydride in particular, opens the door to its use in future fuel cell applications. Keeping the fuel in solid form allows for easy distribution and transportation and maintains the safety factor of low pressures. Also, the precious metal catalyst is replaced by an inexpensive and readily available solid acid such as citric acid. Furthermore, the hydrogen produced by these reactions has been shown not to contain any gases that may poison the fuel cell membrane, and it offers relative humidity near that of 100%. This fuel combination can be scaled as needed to allow this single technology to be used for applications ranging from micro and portable electronics all the way to automotive applications.

Acknowledgements

The author thanks Dr. Bor Jang of Wright State University for his continuing support and funding. He also acknowledges the help and support of his co-workers at Nanotek Instruments.

References

[1] Weblink:http://www1.eere.energy.gov/hydrogenandfuelcells/fuelcells/fc_types.html HFCIT Fuel Cells: Types of Fuel Cells, accessed on 23rd Aug. 2009.

[2] Weblink:http://www.fuelcellmarkets.com/fuel_cell_markets/proton_exchange_membrane_fuel_cells_pemfc: PEM - Proton Exchange Membrane Fuel Cells, accessed on 9th Jul. 2009.

[3] Weblink:http://www1.eere.energy.gov/hydrogenandfuelcells/production/natural_gas.html HFCIT Hydrogen Production: Natural Gas Reforming, accessed on 10th Jul. 2009.

[4] Weblink:http://www1.eere.energy.gov/hydrogenandfuelcells/storage/chem_storage.html HFCIT Hydrogen Storage: Chemical Hydrogen

Storage,. accessed on 22nd Jul. 2009.
[5] S. C. Amendola, "System for hydrogen generation," US Patent no: 6,534,033, 2003.
[6] I. M. Fuller et al., "Method of storing and generating hydrogen for fuel cell applications,". US. Patent Pending:11/784,440, 2007.
[7] Weblink:http://www.argus-hazco.com/ Industrial health, safety and environmental monitoring, accessed on 25th Jul. 2009.

About the Author

Ian M. Fuller is a senior at Wright State University where he is majoring in Engineering Physics. He has spent his college career doing research and development on hydrogen fuel cells and their accompanying equipment as an intern at Nanotek Instruments in Dayton, Ohio. He has received numerous awards for his work from the Ohio Fuel Cell Coalition, Dayton Engineering Sciences Symposium, and also has filed for US Patents. Outside of school and work, Ian is very active in local soccer leagues where he has coached and trained younger players, as well as played on local adult leagues.

Crossword

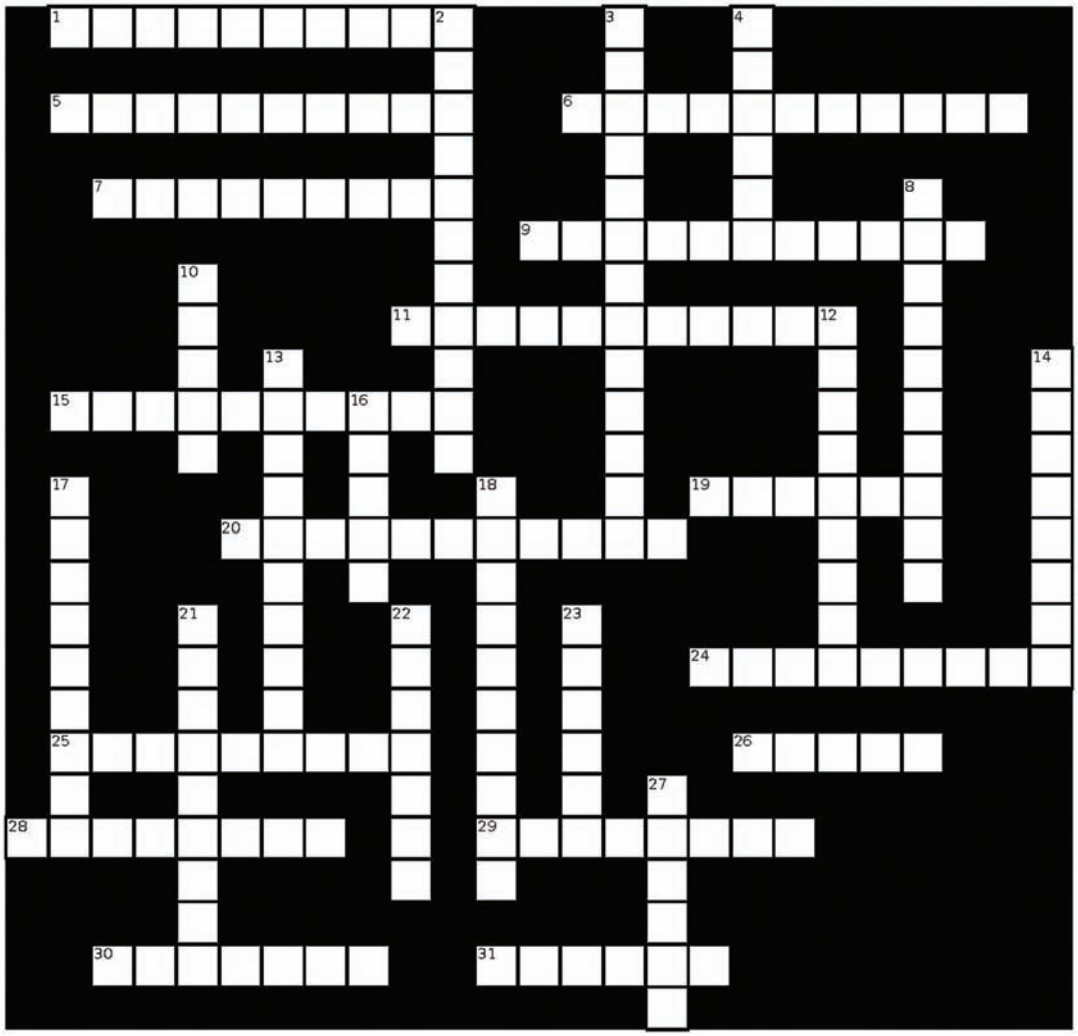

Across

1 Splitting of water molecules into hydrogen cations
5 Memory within a system
6 Opposite of tensile forces
7 Constituent of plant cell walls
9 Ability of a substance to attract water molecules from the surrounding environment
11 Bending of light upon contact with another medium
15 Energy state above the ground state
19 6 stringed instrument
20 Section of electromagnetic spectrum just above visible light wavelengths
24 Surface upon materials can be doposited
25 Lacking definite structure
26 Foot protection
28 Combination of reagents
29 Joining of elements in small groups
30 Mass/Volume
31 Chemical solution proccess

Down

2 Heterogeneous fluid containing solid particles that are sufficiently large for sedimentation
3 Ability to break down within a biological system
4 Void space within a material
8 Polarizable electronic indicator
10 Edge boundary defect
12 Cylinders on the 10^{-9} scale
13 Peak to peak distance
14 Selective barrier
16 Does not interact with surrounding environment
17 Section of electromagnetic spectrum used to cook food
18 Use of light and lens to observe a sample
21 Oscillation of a wave
22 Solid material with a repeating pattern within the struc ture
23 Loose collection of particles
27 Densification

Key is available at *www.jumr.mse.vt.edu.*

Publish. Gain recognition.

Be part of something exciting.

Submit your paper for consideration in Volume 5

If you are an undergraduate student at any institution working on a materials-related project, here is your chance to become published. Your submitted paper will undergo a peer-review for consideration in Volume 5 of the *Journal of Undergraduate Materials Research*.

For submission requirements, see
http://www.jumr.mse.vt.edu

Manuscripts or questions should be sent to
JUMR
213 Holden Hall
Virginia Tech
Blacksburg, VA 24061
jumr@mse.vt.edu

JUMR
213 Holden Hall
Virginia Tech
Blacksburg, VA 24061

Non-profit organization
U.S. Postage PAID
Blacksburg, VA 24060

Permit No. 28